Chapter 4

The Reduction-Coupled Oxo Activation mechanistic motif for C−H bond activation and oxidation

Reproduced in part with permission from:

1. Cheng, M.-J.; Fu, R.; Goddard, W. A. III. *Chem. Commun.* **2014**, *50*, 1748–1750. © 2014 The Royal Society of Chemistry; available at `http://dx.doi.org/10.1039/C3CC47502F`;

2. Cheng, M.-J.; Goddard, W. A. III.; Fu, R.; Nielsen, R. J. *Top. Catal.*, in press. Unpublished work © 2014 Springer.

Also includes original work.

4.1   Abstract

The vanadium phosphorus oxide (VPO) catalyst is used commercially for the selective oxidation of *n*-butane to maleic anhydride. Surprisingly, the mechanism has been shown to initiate with C−H activation by a P=O moiety. In this chapter, we call this phenomenon the *Reduction-Coupled Oxo Activation* (ROA) mechanistic motif, and attribute it to the concomitant formation of a strong oxo-hydrogen bond on the phosphorus atom and a one-electron reduction on the vanadium atom. In addition, we show that the same ROA phenomenon can be extended beyond phosphorus and vanadium to additional main-group elements and transition metals, respectively, and may lead to a new strategy in designing selective catalysts for alkane activation. Finally, we propose the existence of a homogeneous vanadium phosphorus oxo complex that can incorporate the novel ROA mechanistic pathway as a potential propane oxidation catalyst. We considered several oxidation pathways leading to end products such as propylene, isopropanol, and propylene oxide. We support our assertions with density functional theory calculations on potential reaction pathways.

4.2   Introduction

### 4.2.1   The VPO catalyst for n-butane oxidation

Vanadium phosphorus oxide (VPO) is an inorganic complex that catalyzes the oxidation of n-butane to maleic anhydride with a surprisingly high selectivity of 60-70% [1] (Scheme 4.1). Although the overall yield is only $ca.$ 50%, its ease of synthesis, use of common elements, and selectivity have allowed this catalyst to be commercialized, producing $ca.$ 500 kilotons of maleic anhydride annually [2]. Hence, there was a strong impetus to investigate the mechanism of this reaction in the hopes of rationally designing a modified catalyst with improved yield.

Scheme 4.1. The oxidation of n-butane to maleic anhydride using vanadium phosphorus oxide as a catalyst.

A useful parameter for the C−H activating ability of each oxo moiety in the catalyst is the H-atom affinity D_H, which is defined as the enthalpy change when the O−H bond in ·M−O−H is homolytically cleaved to form the M=O oxo. Mechanistic work initially centered on vanadyl pyrophosphate $((V^{IV}O)_2(P_2O_7)$, abbreviated VOPO), the major component of VPO [3]. However, it was quickly found that no vanadium oxo on the VOPO surface has sufficient H-atom affinity to activate n-butane (Figure 4.1). The most active V=O in VOPO has a D_H value of 58.2 kcal/mol, whereas the weakest C−H bond in n-butane has a dissociation energy of 89.3 kcal/mol, implying an extremely endothermic first step that is categorically inconsistent with the experimentally determined activation energy of 12.9-23.6 kcal/mol [4]. Hence, it was concluded that the reduced vanadyl pyrophosphate $(V^{IV}O)_2(P_2O_7)$ alone is unable to initiate the catalytic process.

Figure 4.1. O−H bond strength for oxygen atoms on the $(V^{IV}O)_2(P_2O_7)$ surface. The energy released when an H · is bound to the V=O (in red) is only 58.2 kcal/mol, not nearly high enough for alkane activation to occur. The energy released when an H · is bound to the bridging V−O−P oxide (in green) is even lower, at 17.0 kcal/mol. The energy released when an H · is bound to the P=O was not determined because geometry optimization caused it to be transferred to the V−O−P moiety (in green).
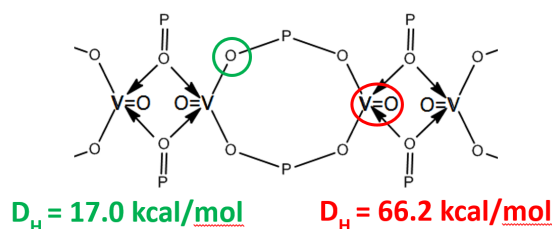
It was then supposed that catalysis requires the presence of adsorbed O_2 on the $V^{IV}O(P_2O_7)$

surface. Adsorption of O_2 may be molecular, in which the $O-O$ bond is retained, two V^{IV} centers are oxidized to V^V, and a vanadium peroxo moiety is formed; or it may be dissociative, in which the $O-O$ bond is broken and four V^{IV} centers are oxidized to V^V. The first case is uphill by 2.8 kcal/mol, whereas the second is downhill by 38.8 kcal/mol. Unfortunately, the D_H values calculated for the resulting vanadium peroxo and vanadium oxo moieties were only 70.0 and 58.9 kcal/mol, respectively. Hence, it was concluded that the reduced VPO complex is not the active catalyst.

Figure 4.2. Oxygen adsorption energies on the $(V^{IV}O)_2(P_2O_7)$ surface and the $O-H$ bond strength (D_H) to each of these O atoms. Left: molecular O_2 adsorption in which the $O-O$ bond is preserved. Right: dissociative adsorption in which the $O-O$ bond is broken. All energies are in kcal/mol.
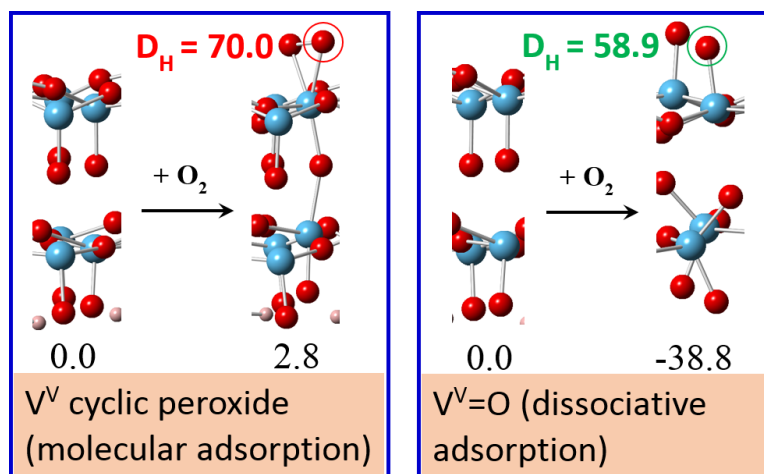
Finally, it was proposed that catalysis takes place on a metastable V^VOPO_4 surface, known as the X1 phase, which has been experimentally determined to be produced in the high oxygen environment of the reaction conditions [5]. However, the largest D_H value found for a vanadium oxo in this phase is only 62.8 kcal/mol (Figure 4.3). Surprisingly though, it was discovered that the phosphorus oxo had a much larger D_H value of 84.3 kcal/mol! This implies a first step that is endothermic by only 5.0 kcal/mol, with an activation energy later calculated to be 13.6 kcal/mol, which is within the experimental range. The stability of the resulting monohydrogenated species was attributed to the fact that spin density appears to be localized on the neighboring vanadium atoms (Figure 4.4).

4.2.2 The ROA mechanistic motif

The surprising discovery of the $C-H$ activation ability of $P^V=O$ moieties in the V^VOPO_4 catalyst led to the creation a new term, *Reduction-Coupled Oxo Activation* (ROA), to describe this phenomenon. Its usefulness is due to the observation that the basicity of simple transition metal oxos increases with decreasing electron affinity of the metal, due to increasing electron density; whereas for $C-H$ activation it is preferred that both basicity and electron affinity are maximized, since H-atom transfer

Figure 4.3. O−H bond strengths for the various oxygen atoms on the X1-V^{V}OPO$_4$ surface. The O−H bond strength of 84.3 kcal/mol to the P=O moiety leads to a first step that is endothermic by only 5.0 kcal/mol, with an activation energy later calculated to be 13.6 kcal/mol. Hence, the P=O moiety is the only candidate site whose C−H activation energy is compatible with experimental data.
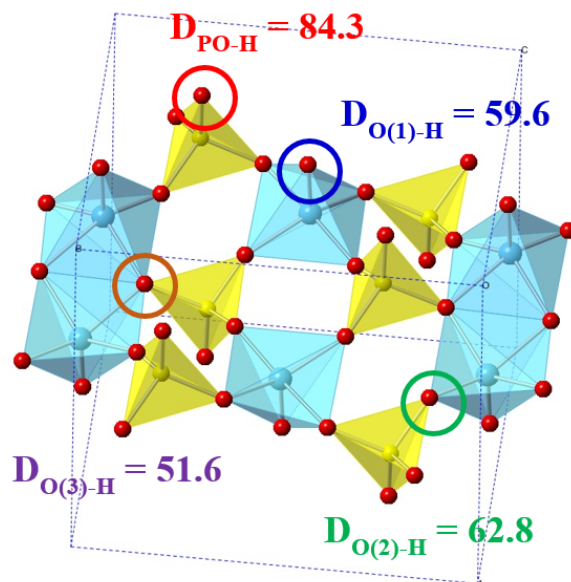

Figure 4.4. C−H activation by a phosphorus oxo leads to a one electron reduction on the neighboring vanadium. Hence the oxidation state of the phosphorus atom does not change. (a) Vanadium-phosphate archetype: conceptual arrow-pushing scheme for P−V electron transfer with an intervening μ−oxo. (b) Vanadium-κ−P-phosphinite archetype: conceptual arrow-pushing scheme for P−V electron transfer in which they are directly bound to each other.
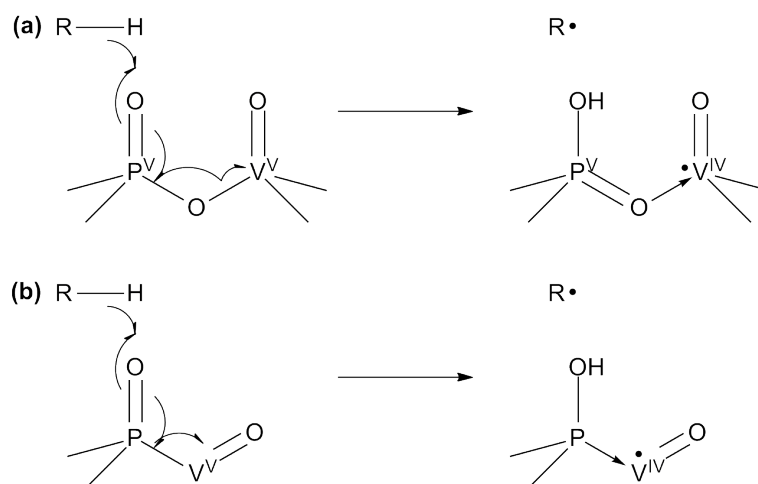
involves both proton and electron transfer. The ROA mechanistic motif, by keeping the sites of basicity and reduction on separate moieties, is able to decouple this process and hence allow the best of both worlds with high basicity and high electron affinity [6].

The validity of the ROA mechanistic motif was tested using quantum mechanical calculations on small X_4O_{10} clusters, where each X is a P or V. The results, shown in Figure 4.5, indicate that a single linkage to V makes the P=O bond 32.3 kcal/mol more active, while coupling to a second V makes it an additional 23.8 kcal/mol more active and coupling to a third V (as in VPO) makes it an additional 4.9 kcal/mol more active. Compared to a pure vanadium (V) oxide case, coupling to one or two P atoms makes it 13.4 and 8.5 kcal/mol more active, respectively.

Figure 4.5. Use of finite cluster models to investigate how the O−H bond strength of P=O moieties varies based on the number of V coupled to it *via* O linkages. Data is summarized from Figure 4.8. All numbers are in kcal/mol.

|	Species	$D_{PO(1)-H}$
a.	P_4O_{10}	28.2
b.	P_3VO_{10}	60.5
c.	$P_2V_2O_{10}$	84.3
d.	PV_3O_{10}	89.2
e.	V_4O_{10}	75.8
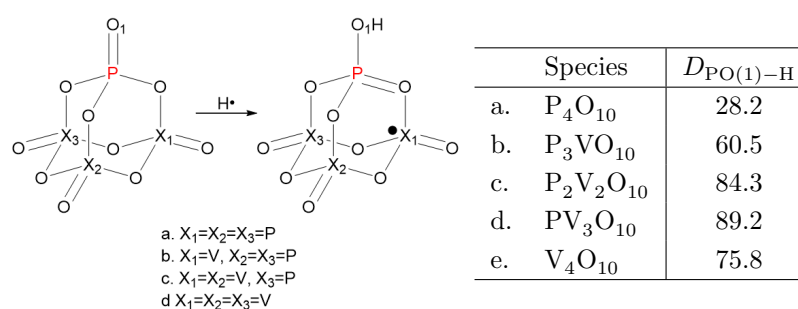
The data presented in Figure 4.5 shows the validity of the small cluster approach in gauging the activity of the ROA mechanism. In hopes of expanding the chemical space in which this ROA mechanism is available, we have undertaken an investigation of mixed oxos with vanadium and the heavier group 15 (pnictogen) and 16 (chalcogen) elements in the first part of this chapter. (We do not consider group 14 or 17 elements due to the instability of terminal oxos for such elements, against hydration in the group 14 case and explosion in the group 17 case.) For each of these complexes, we have calculated D_H, the oxo-hydrogen bond energy. We use D_H as a proxy for hydrogen-abstraction potential, which is typically the most difficult step in alkane oxidation/functionalization catalysis. We have found that the ROA mechanism is general to group 15 and 16 (pnictogen and chalcogen) vanadium mixed oxos, with phosphorus, selenium, and tellurium being the most active. We have also taken these most active cases, with molybdenum (VI) substituted for vanadium (V), and found similarly promising results. We hence conclude that the reduction-coupled oxo activation mechanistic motif is a viable and interesting new lead for the development of new oxidation catalysts.

4.2.3 Potential homogeneous catalysts utilizing the ROA principle

Although the ROA phenomenon was originally discovered in the VPO system, a heterogeneous catalyst, the principle should hold for homogeneous catalysts as well. Homogeneous catalysts have the advantages of being well-defined, easier to study, and thus more readily able to contribute to basic scientific research. However, homogeneous complexes containing a $P(O)-O-V(O)$ moiety (as shown in figure 4.4a) are very rare in the literature, owing to their difficulty in synthesis [7]. The only known examples are complexes produced by Herron et al. [8] and Cummins et al. [9], both of which were simply precursors to the production of VOPO or related network complexes; and the very recent work by Doyle et al. [7] that features the divanadium pyrophosphate complex $\{[(V^{IV}O)bipy(H_2O)]_2(\mu-P_2O_7)\} \cdot 3\,H_2O$, which exhibits some catalytic oxidative ability with benzyl alcohol. Hence, potential catalysts incorporating an alternative metal core featuring a direct $V-P$ bond (as in figure 4.4b) were explored. Complexes featuring such $\kappa-P$ phosphinite coordination to metals including Co [10], Ni [11]a, Pd [11], and Pt [12]a have been described. In addition, many other complexes containing a phosphido ligand bonded to metals such as Co [10], Rh [12]b, Pd [12]bc, Ir [13], and Pt [12]abd have also been described. These phosphido complexes are a single monooxygenation step away from the corresponding phosphine oxide complexes, a transformation which is expected to be facile due to the large formation energy of phosphine-oxo bonds and which has in fact been reported for a few of the complexes [10, 12]a. However, since in all these complexes the metal center has been from the late row transition metals, they are not predicted to be effective alkane activation catalysts under the ROA mechanism due to their large number of d electrons.

In order to design a homogeneous oxidation catalyst that utilizes the ROA mechanistic motif, a natural choice for the metal center of a phosphine-oxide-type complex would once again be vanadium (V), due to its activity in the VPO catalyst and its status as an effect d^0 one-electron acceptor. The existing metal $\kappa-P$ phosphinite and phosphido complexes all feature shared traits such as a late transition metal in a low oxidation state and a phosphorus moiety incorporated as the center of a tricoordinate pincer ligand with flanking phosphines and aryl linkers. Such ligands, which were designed for late transition metals, would likely not form very stable complexes with an early transition metal such as vanadium. However, replacement of the ligand's side phosphines with harder oxygens would be expected to greatly improve stability. Hence, we propose the ligand bis(2-phenoxyl)phosphinite $\kappa-P$ coordinated on vanadium, abbreviated (OPO)V, as our candidate catalyst, in analogy to the existing Pd complex [11] (Figure 4.6). The robustness of this complex is predicted based on factors such as the chelation effect, the stability of $O-V$ bonds, and the rigidity of the ligand, which guards against insertion of small activating molecules into the $V-P$ bond. We complete the first coordination sphere around V by noting that it prefers to be six-coordinate and to contain a strong vanadium oxo bond [8], and we fill in the last open coordination sites with aqua ligands.

Figure 4.6. Left: known complexes featuring a phosphinite ligand bound $\kappa-P$ to a transition metal. Right: A proposed vanadium $\kappa-P$ phosphinite complex $(OPO)VOL_2$. In aqueous solution or when water is present in the system, L is H_2O. Note that both *fac* and *mer* stereoisomers are possible.
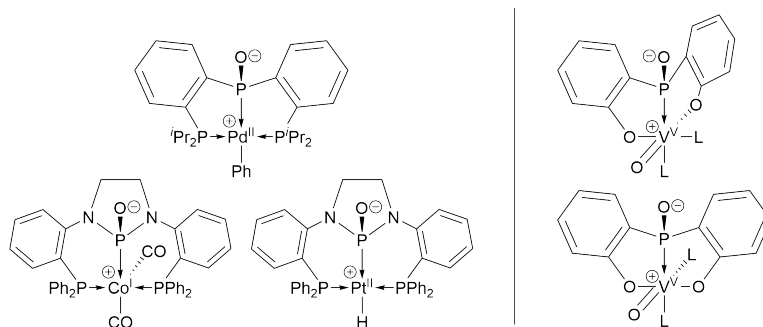
We thus propose, in the second part of this chapter, that the hypothetical complex diaqua[bis(2-phenoxy)phosphinite-$\kappa-P$]oxidovanadium (V) $((OPO)V^VO(H_2O)_2)$ utilizes the reduction-coupled oxo activation (ROA) mechanistic motif as a catalyst for the oxidation of alkanes in air. In this proposition, we support our assertion with density functional theory (DFT) calculations of the various reaction paths starting from propane, our representative alkane. We describe the most plausible transition state barriers for the conversion of propane and dioxygen to oxidized products such as propylene and isopropanol. Through our theoretical findings we are confident that a realized molecule will hold catalytic ability in a manner heretofore unseen in homogeneous catalysis.

4.3 Materials and methods

All quantum mechanical calculations were carried out using the Jaguar software version 7.9 developed by Schrödinger Inc. [14]. Geometry optimizations were carried out on initial guess structures, and vibrational frequencies were gathered to confirm the optimized geometries as intermediates or transition states and to construct a free energy profile. The temperature was set to be 298.15 K. Solvation energies were calculated in water using the PBF Poisson-Boltzmann implicit continuum solvation model [15] in Jaguar, with a dielectric constant of 80.37 [16] and a probe radius of 1.40 Å [17] for water. Two explicit solvating waters per aqua, hydroxo, or oxo ligand were added for more accurate solvation modeling.

For our proposed molecular catalysts, geometry optimization and vibrational data were calculated using the B3LYP density functional [18] with a smaller basis set, whereas single point gas-phase and solvated energies were calculated using the same functional and a larger basis set. Here the smaller basis set consists of a modified double-ζ Los Alamos basis set and pseudopotential (LACVP**) [19] for transition metals, the uncontracted Los Alamos valence-only basis set and pseudopotential (LAV3P) [20] for heavy main-group elements (e.g., As, Se, Sb, Te, Bi), and the

6-31G** basis set [21] for the other atoms; whereas the larger basis set consists of the triple-ζ Los Alamos basis set and pseudopotential (LACV3P**++) for transition metals, the same LAV3P basis set and pseudopotential for heavy main-group elements, and the 6-311G**++ basis set [21] for the other atoms. Proposed intermediates and transition states were found to have zero and one negative frequencies, confirming their status as local energy minima and saddle points, respectively.

The pH of the aqueous solution was set at 0 or 7; this corresponds to the free energy of a solvated proton being set as -270.28 or -279.80 kcal/mol, respectively [22].

The free energy for each molecular species in solution was calculated using the formula

$$G = E_{\text{gas}} + \Delta G_{\text{solv}} + \text{ZPE} + H_{\text{vib}} + 6kT - T[S_{\text{vib}} + \gamma(S_{\text{trans}} + S_{\text{rot}} - \alpha) + \beta]$$

where the last term (with $\alpha = 14.3$ e.u., $\beta = 7.98$ e.u., and $\gamma = 0.54$) is an empirical approximation for the change in the translational and rotational entropy of the molecule between the gas phase and the solution phase (due to the finite librational frequencies), derived from Wertz [23].

For gas phase molecules (H_2, O_2, propylene, propane, and for our purposes the isopropyl radical), we assumed that equilibration between the dissolved gas and the headspace occurs at a much faster timescale than the reactions in question; leading to $\Delta G_{\text{gas} \rightarrow \text{solv}} = 0$. Thus, the free energy of such gas molecules can be simply calculated using the formula

$$G = G_{\text{gas}} = E_{\text{gas}} + \text{ZPE} + H_{\text{tot}} - TS_{\text{tot}}.$$

For water, the Gibbs free energy was calculated using the formula

$$G_{\text{liquid}} = E_{\text{gas}} + \text{ZPE} + H_{\text{tot}} - TS_{\text{tot}} + \Delta G_{\text{gas} \rightarrow \text{liquid}}$$

where $\Delta G_{\text{gas} \rightarrow \text{liquid}} = G_{\text{liquid}} - G_{\text{gas}}(1\text{atm})$ is the free energy of condensation to liquid from 1 atm gas. We can solve for this by noting that

$$\Delta G_{\text{gas} \rightarrow \text{liquid}} = \Delta G_{\text{expansion}} + G_{\text{gas} \rightarrow \text{solvation}},$$

where $\Delta G_{\text{expansion}} = G_{\text{gas}}(P) - G_{\text{gas}}(1 \text{ atm})$ is the expansion of the gas from 1 atm to the vapor pressure P, and $G_{\text{gas} \rightarrow \text{solvation}}$ is the condensation of gas at vapor pressure P to liquid. Since a liquid is by definition at equilibrium with its vapor pressure $G_{\text{gas} \rightarrow \text{solvation}} = 0$, and we thus have

$$\Delta G_{\text{gas} \rightarrow \text{liquid}} = G_{\text{gas}}(P) - G_{\text{gas}}(1 \text{ atm}) = RT \ln\left(\frac{P}{1 \text{ atm}}\right).$$

The vapor pressure of water at 298.15 K is 23.75 mmHg [24].

For a given species X and its monohydrogenated analogue XH$\cdot$, the D_{H} value is defined as

$D_H = H(X) + H(H \cdot) - H(XH \cdot)$, and the G_H value is defined analogously.

For our small cluster calculations, only gas phase energies and frequencies were calculated using the smaller basis set.

4.4 Validation of ROA on small oxide clusters

We performed our calculations on small oxide clusters (Figure 4.7), which we used as models for large inorganic network systems. Restricting our investigation to small discrete clusters allowed us to perform highly accurate *ab initio* quantum mechanical computations.

Figure 4.7. General models for small oxide clusters. (a) X is a pnictogen in the +V oxidation state; (b) Z is a chalcogen in the +VI oxidation state; (c) Z is a chalcogen in the +IV oxidation state. The oxidation state of each vanadium is +V before hydrogen atom abstraction and either +V or +IV after a hydrogen atom has been adducted.
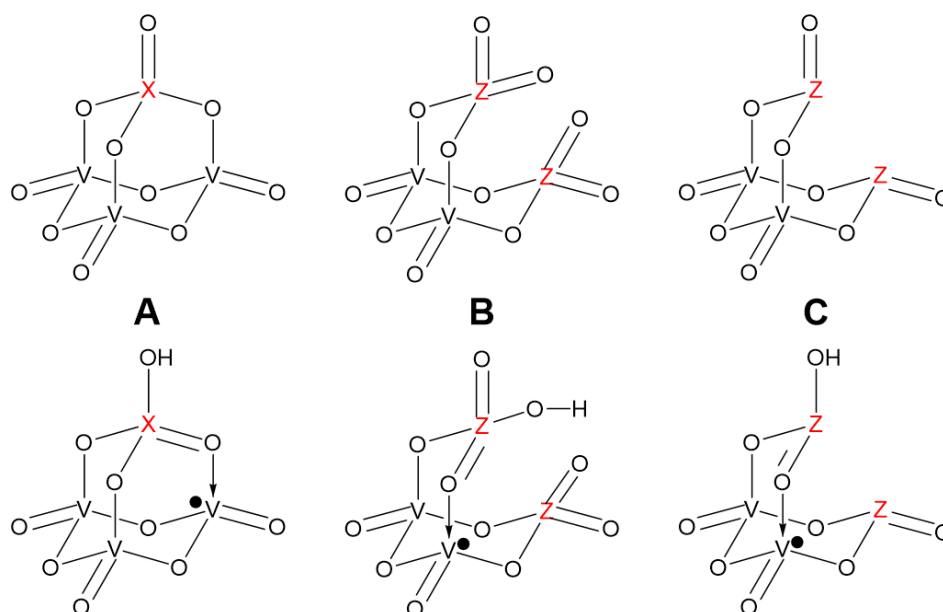
We begin with X = V, an all-transition metal cluster that will serve as a control. The first column of Figure 4.8 shows the structure of both the non- and monohydrogenated forms. Note that the D_H value of 75.8 kcal/mol is already significantly high, owing to the naturally effective oxidizing potential of vanadium in the +V oxidation state.

Replacing one vanadium atom with phosphorus (Figure 4.8, second column), we find that the D_H energy has strengthened by 13.4 kcal/mol, to 89.2 kcal/mol. This is the canonical example of our reduction-coupled oxo activation mechanism. Replacing a second vanadium with phosphorus (Figure 4.8, third column) gives a slightly reduced, but similar D_H value of -84.3 kcal/mol. Compared to the experimental results in [3], in which the phorphoryl site has a D_H value of 84.3 kcal/mol,
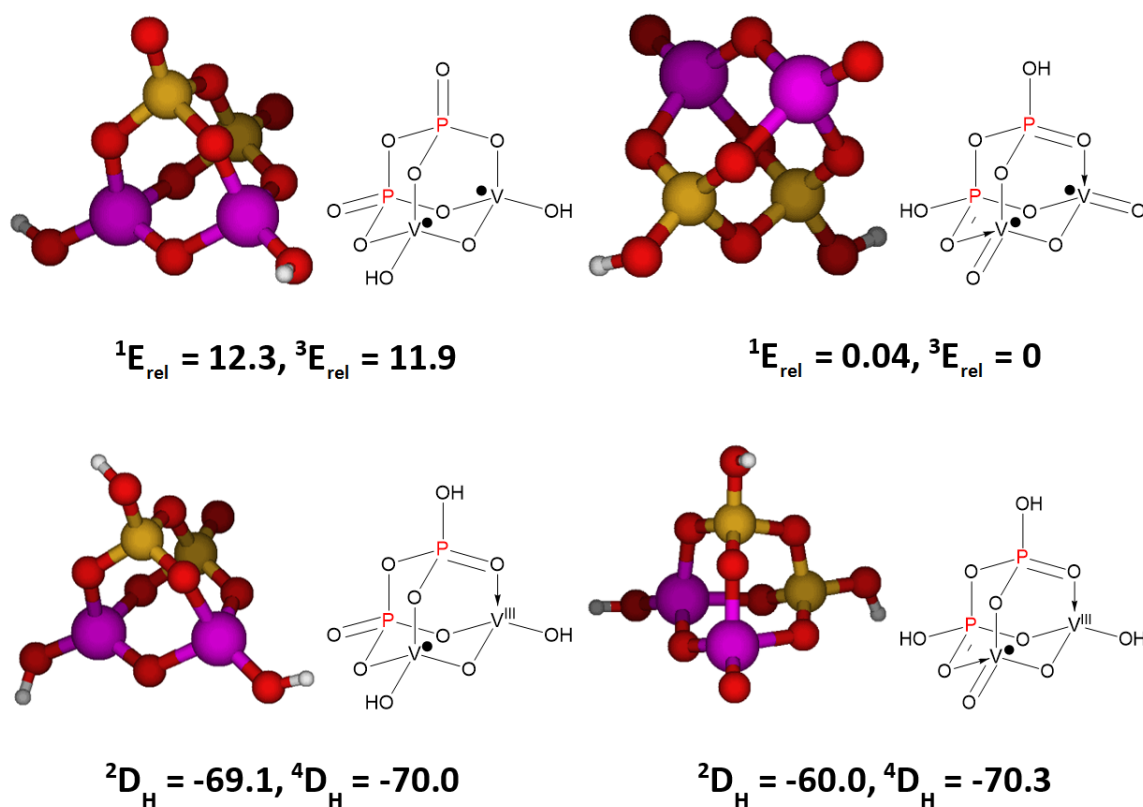
Figure 4.8. Optimized structures of the $P_xV_{4-x}O_{10}$ species (first row) ($x \in \{0, 1, 2, 3\}$) and their schematic representations (second row); optimized structures of the monohydrogenated $P_xV_{4-x}O_{10}H$ species (third row) and their schematic representations (fourth row). Mulliken spin density was used to assign radical character. All numbers are in kcal/mol.
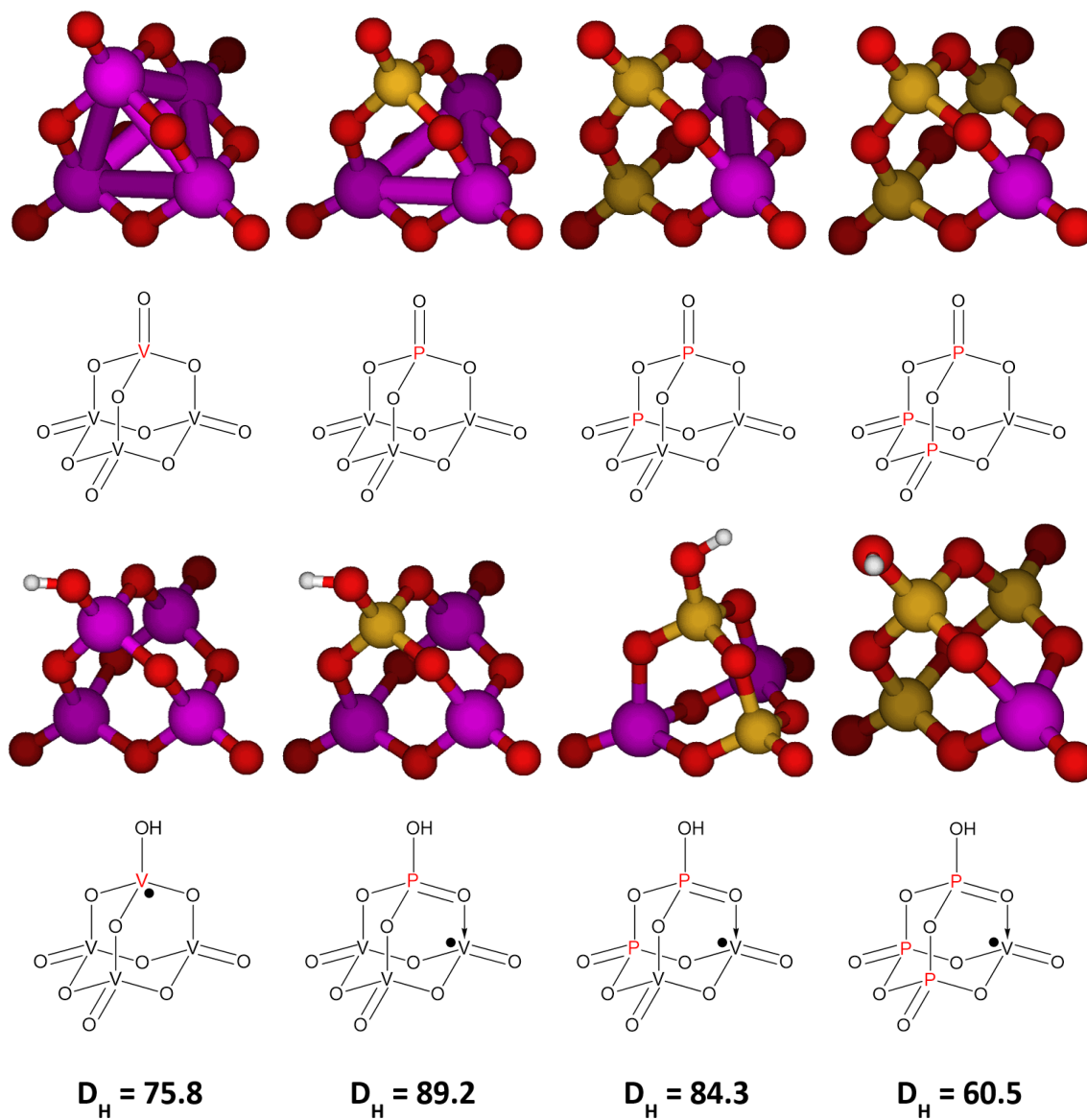
these numbers are a good validation for our cluster model.

We also examined the $P_2V_2O_{10}H_2$ cluster, i.e. the dehydrogenated version. As the first row of Figure 4.9 indicates, regardless of the location of the hydrogen atoms, it is always the two vanadiums that are reduced to +IV. However, it is preferable by about 12 kcal/mol to attach the hydrogens onto the phosphoryl groups, due to the special stability of the vanadyl unit. The unpaired spins on each V^{IV} are essentially independent, as there is almost no difference in energy or geometry between the singlet and triplet in both cases. We found that addition of a third hydrogen to the system always reduces one vanadium atom to +III, leading to either an overall doublet (doublet V^{IV} and singlet V^{III}) or an overall quartet (doublet V^{IV} and triplet V^{III}). The phosphorus atoms, in a sign of their resistance to reduction, stay in the +V oxidation state in all cases. The lack of V^V centers compared to the case in Figure 4.8 accounts for the significant reduction in D_H values.

Figure 4.9. Optimized structures of the dihydrogenated $P_2V_2O_{10}H_2$ species (first row), their schematic representations, and their energy relative to the lowest isomer; optimized structures of the trihydrogenated $P_2V_2O_{10}H_3$ species (second row). Only the triplet and quartet structures are shown because the singlet and doublet structures are almost identical to them. Mulliken spin density was used to assign radical character. All numbers are in kcal/mol.

$^1E_{rel} = 12.3, ^3E_{rel} = 11.9$

$^1E_{rel} = 0.04, ^3E_{rel} = 0$

$^2D_H = -69.1, ^4D_H = -70.0$

$^2D_H = -60.0, ^4D_H = -70.3$

Having established the validity of our model, we now endeavored to survey the span of the group 15 (pnictogen) vanadium (V) oxides. We found that when going down the periodic table, from phosphorus to arsenic to antimony, the D_H energy decreases (Figure 4.10). Bismuth, the last

element in the series, has an D_H that is slightly higher than antimony above it, but it is still not as effective as a pure vanadium-oxygen cluster and furthermore is too susceptible to reduction to the +III state.

Figure 4.10. Optimized structures of the XV_3O_{10} species (first row) (X $\in$ {P, As, Sb, Bi} and their mono-hydrogenated $XV_3O_{10}H$ counterparts (second row). Schematic structures are as in Figure 4.7a. Mulliken spin density was used to assign radical character. All numbers are in kcal/mol.

$$D_H (P) = 89.2 \qquad D_H (As) = 79.1 \qquad D_H (Sb) = 63.8 \qquad D_H (Bi) = 67.9$$
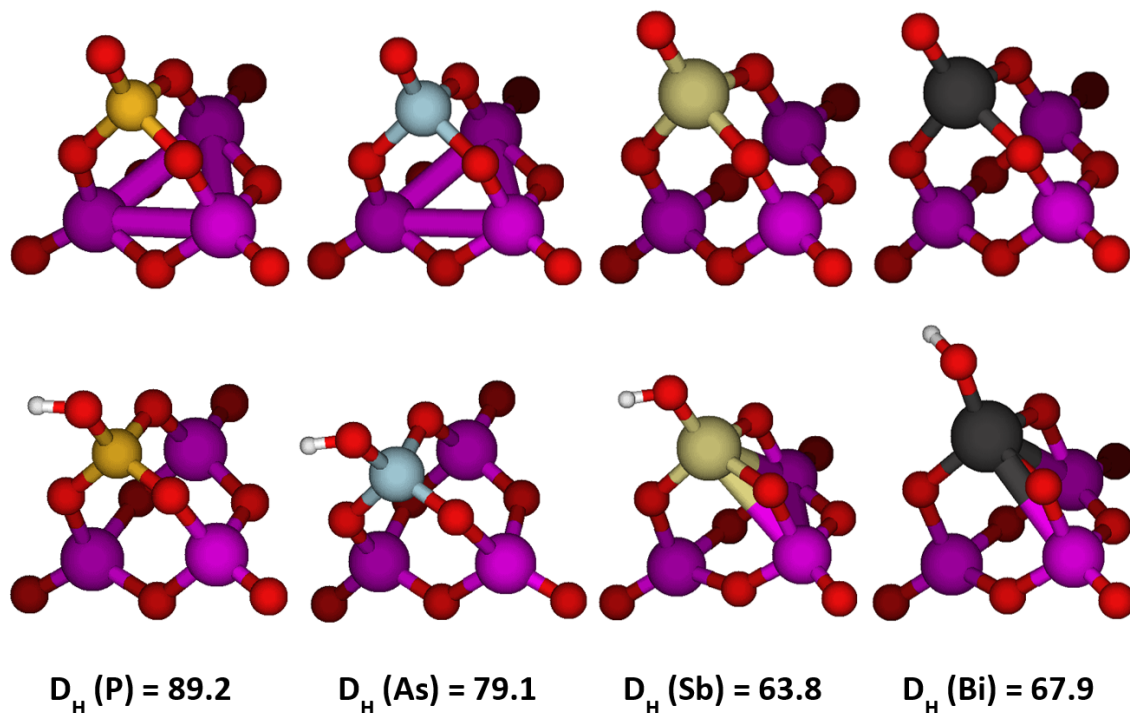
We also examined the potential group 16 (chalcogen) vanadium (V) oxides, in clusters as depicted in Figure 4.7bc. We found that for sulfur, selenium, and tellurium in the maximum +VI oxidation state, all structures had D_H values of 90 kcal/mol or greater (Figure 4.11). We view this as a very promising potential direction for new catalysts.

It is well documented that tellurium prefers higher coordination numbers; for example, unlike its lighter cogeners, the hydrated H_6TeO_6 is stable whereas the four-coordinate H_2TeO_4 is unknown. Examining several potential structures for the hydrated complex $Te_2V_2O_{12}H_2$, we found that the lowest energy conformation had a hydration energy of 6.3 kcal/mol downhill. The resultant structure (Figure 4.12) has a bridging μ-oxo that renders the two tellurium atoms five coordinate, and a proton on an oxygen atom on each tellurium. The lowest conformation of the corresponding monohydrated complex $Te_2V_2O_{12}H_3$ gave a D_H value of 92.0 kcal/mol, very comparable to the dehydrated complex. Upon hydrogen atom abstraction the μ-oxo breaks, resulting in only one of the tellurium atoms remaining five-coordinate.

Unfortunately, it appears that there is a strong drive to fully hydrate the complex until both

Figure 4.11. Optimized structures of the $Z_2V_2O_{11}$ species (first row) ($Z \in \{S, Se, Te\}$) and their monohydrogenated $Z_2V_2O_{11}H$ counterparts (second row). Schematic structures are as in Figure 4.7b. Mulliken spin density was used to assign radical character. All numbers are in kcal/mol.
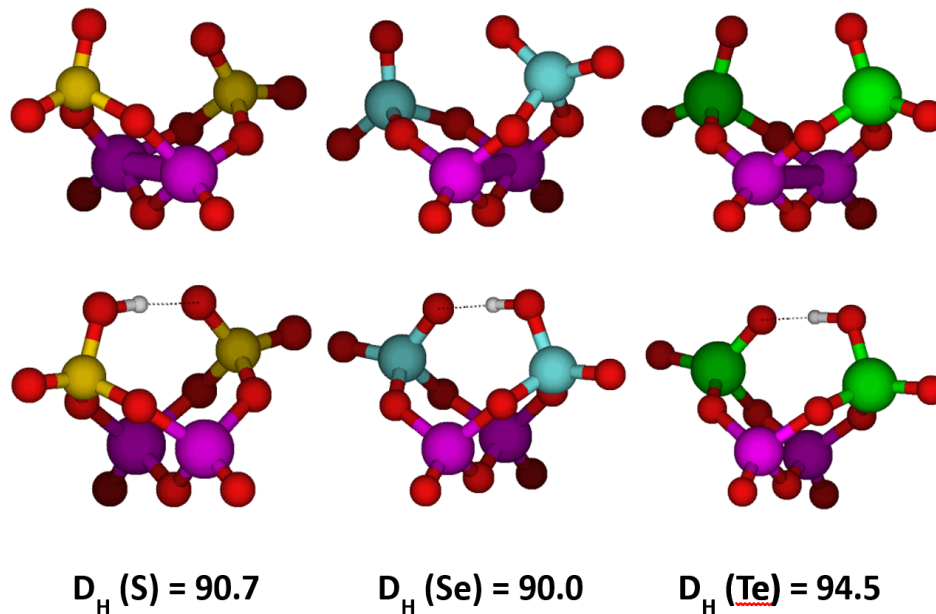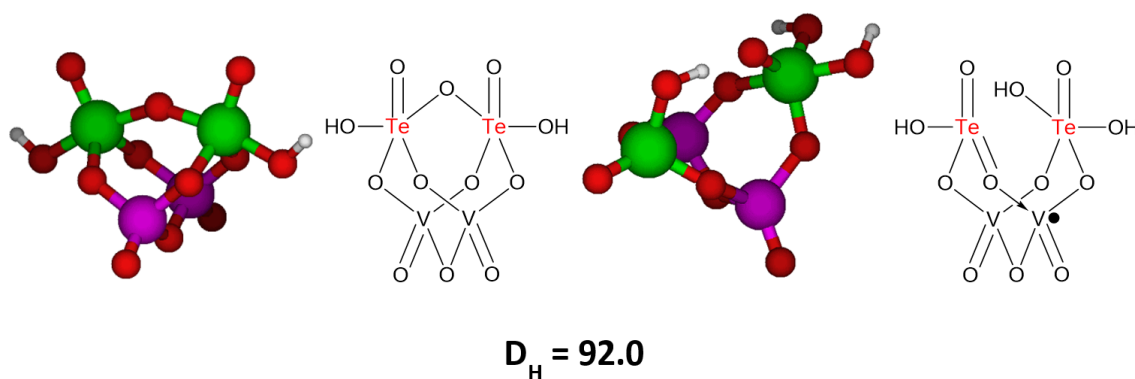

$D_H (S) = 90.7 \qquad D_H (Se) = 90.0 \qquad D_H (Te) = 94.5$

Figure 4.12. Optimized structures of the hydrated species $Te_2V_2O_{12}H_2$ and $Te_2V_2O_{12}H_3$, along with their schematic representations. Mulliken spin density was used to assign radical character. $D_H = 92.0$ kcal/mol.

$D_H = 92.0$

tellurium atoms are six-coordinate: $Te_2V_2O_{11} + 3\,H_2O \longrightarrow Te_2V_2O_{14}H_6$, $\Delta E = -49.2$ kcal/mol. The six-coordinate complex lacks terminal tellurium oxos that can easily abstract hydrogen atoms. Hence, the D_H values are much less, diminished to about 60 kcal/mol. Attachment of a hydrogen atom onto a tellurium hydroxide results in water loss, and is not energetically more favorable than attachment onto a bridging oxo (Figure 4.13). The implication of this is that any putative catalyst incorporating tellurium in the +VI oxidation state will be poisoned by water and will need to be kept in dry conditions.

Figure 4.13. Optimized structures of the fully hydrated species $Te_2V_2O_{14}H_6$ and $Te_2V_2O_{14}H_7$ (first row), along with their schematic representations (second row). Mulliken spin density was used to assign radical character. All numbers are in kcal/mol.
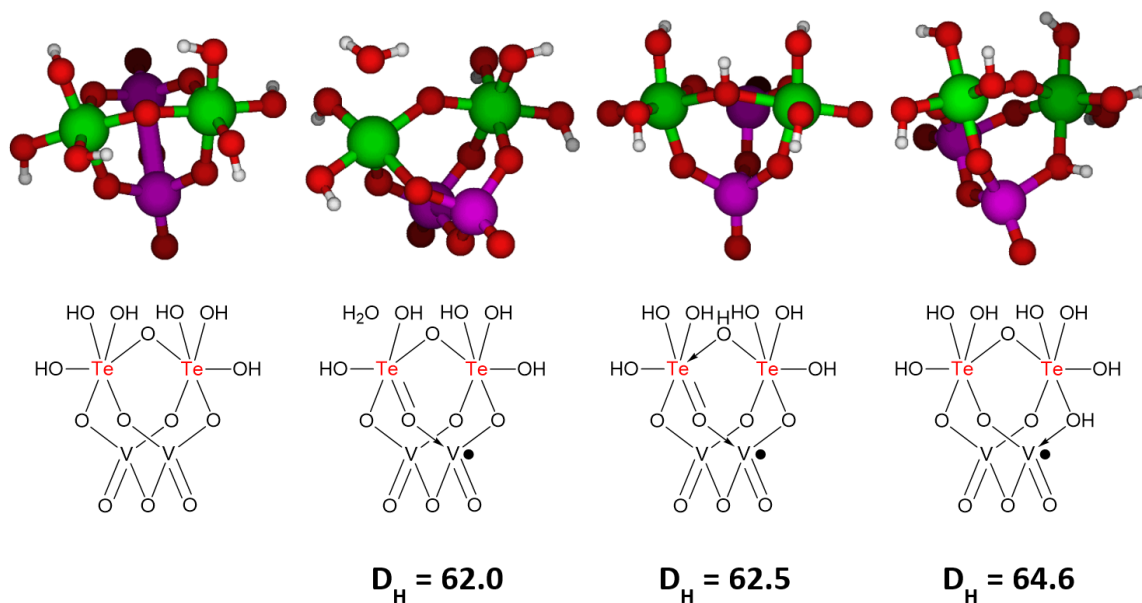
As Se^{VI} and Te^{VI} are both easily reduced to the +IV oxidation state, we also investigated whether vanadium oxide clusters incorporating Se^{IV} and Te^{IV} might also have good hydrogen abstraction capability. Using the structures in Figure 4.7c to build our model, we found that the complexes $Se_2V_2O_9$ and $Te_2V_2O_9$ are also very strong hydrogen atom abstractors (Figure 4.14). In fact, $Te_2V_2O_9$ has a D_H value of 100.0 kcal/mol, the strongest value we have seen. We note that abstraction of one hydrogen atom on a tellurium oxo causes the other tellurium oxo to convert to a bridging oxo, rendering the first tellurium five-coordinate. This is not seen in the selenium case.

We also investigated the activity of vanadium oxide clusters with the group 14 elements Si, Ge, Sn, and Pb in the +IV oxidation state (Figure 4.15). Construction of a cluster model analogous to the templates found in Figure 4.7 results in the complexes $Z_2V_2O_{10}H_2$, where Z = Si, Ge, Sn, or Pb, which are shown in the first row of Figure 4.7. Note that unlike the group 15 and 16 cases, the base $Z_2V_2O_{10}H_2$ clusters do not have any terminal oxo functionalities. This is reasonable and consistent

Figure 4.14. Optimized structures of $Se_2V_2O_9$ and $Te_2V_2O_9$ and their schematic representations (first row); optimized structures of the monohydrogenated $Se_2V_2O_9H$ and $Te_2V_2O_9H$ (second row). Mulliken spin density was used to assign radical character. All numbers are in kcal/mol.

$D_H = 92.2$ $D_H = 100.0$
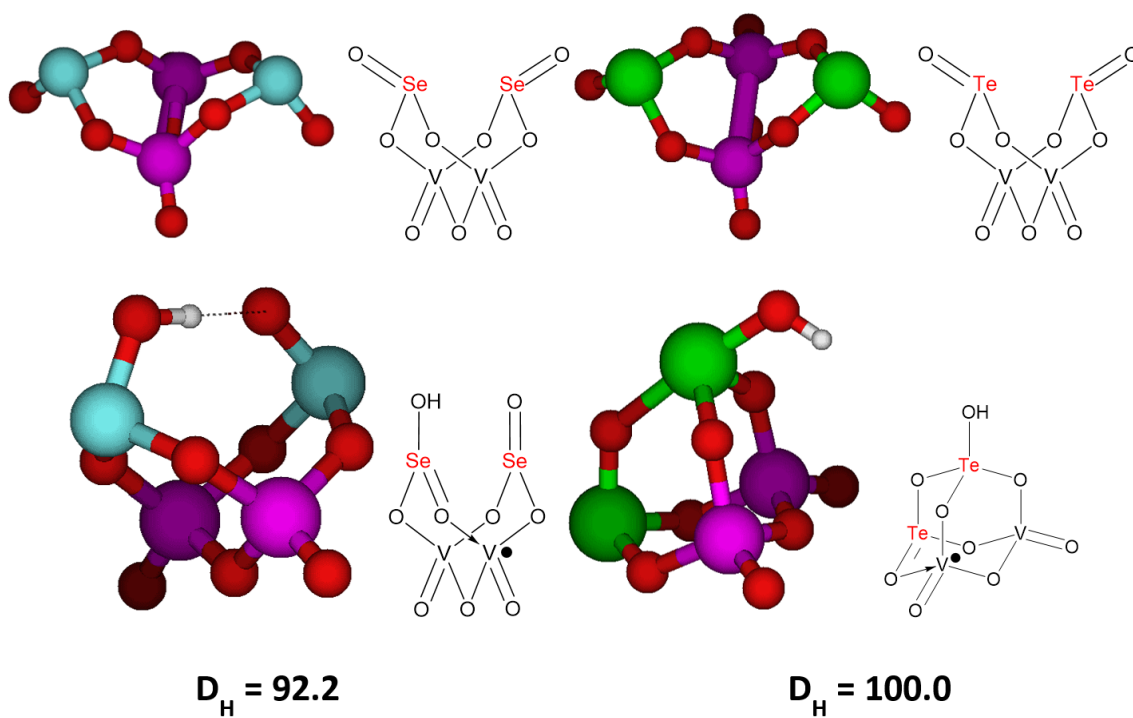
with the common knowledge that group 14 elements other than carbon greatly prefer two single bonds with oxygen over one double bond. Unfortunately, the lack of such terminal oxos results in the inapplicability of the ROA mechanism towards these types of compounds. Hence, the location on each $Z_2V_2O_{10}H_2$ species that results in the greatest amount of energy released when H $\cdot$ is bound is a V=O moiety. The D_H are similar to that of V_4O_{10} (Figure 4.8). Placement of the H $\cdot$ atom on a Z−OH moiety or bridging oxygen resulted in decomposition of the cluster for the cases of Z = Ge, Sn, and Pb; and led to much smaller D_H values for the case of Z = Si. Hence we conclude that the ROA mechanistic motif does not likely extend to the group 14 elements.

Although our work presented up to now have all involved vanadium as the transition metal that absorbs the spin density, we were also desirous of expanding the breadth of our ROA principle to other transition metals. Hence, we decided to take our best cases, involving phosphorous, selenium, and tellurium, and substitute in Mo^{VI} for V^{V}. Unfortunately, we were not able to find a stable structure for monohydrogenated selenium complexes. Our data for phosphorous and tellurium are presented in Figure 4.16.

It can be seen from the data in Figure 4.16 that the activity of phosphorus and tellurium (VI) species are comparable to those with vanadium, but the tellurium (IV) species is ineffectual. This may be due to the two tellurium atoms being too far apart for an oxygen atom to bridge in the same manner as the vanadium case. Nevertheless, we have demonstrated that the ROA pathway which characterizes vanadium (V) chemistry can also be extended to molybdenum (VI).

Whereas calculations on the periodic system appear to show that the spin is delocalized [3], for our cluster calculations, in all cases the spin is not shared, but localized on one atom. This discrepancy may be explained by noting that those prior calculations were made using the PBE density functional, which has been documented to have a bias towards delocalized systems. Regardless, we were able to see the same increased D_H effect without spin delocalization, so that cannot the physical reason behind our ROA mechanism.

Given the observation that main group-vanadium oxide clusters with only certain elements have an increased hydrogen abstraction energy relative to a vanadium oxide cluster alone, it would appear that increases in hydrogen abstraction energy *via* the ROA motif is element-specific and not due to any general chemical principle. For pnictogen vanadium oxide clusters, the only viable candidate was phosphorus, whereas all the chalcogens exhibited similar high activity, especially selenium and tellurium in the +IV oxidation state. These observations cannot be explained by simple periodic trends.

Similar complexes with group 14 elements were not included in this chapter due to the lack of notable positive results. This may be for the same reason as why a fully hydrated tellurium (VI) complex was also poor, due to the lack of an oxo ligand.

Figure 4.15. Optimized structures of the group 14-vanadium oxide species $Z_2V_2O_{10}H_2$, where $Z \in$ $\{Si, Ge, Sn, Pb\}$ (first row); along with their schematic representations (second row). Optimized structures of the corresponding monohydrogenated species (third row) and their schematic representations (fourth row). Alternative locations for $H\cdot$ addition, as well as the corresponding D_H energies, are shown in the fifth row for $Z = Si$. Mulliken spin density was used to assign radical character. All numbers are in kcal/mol.
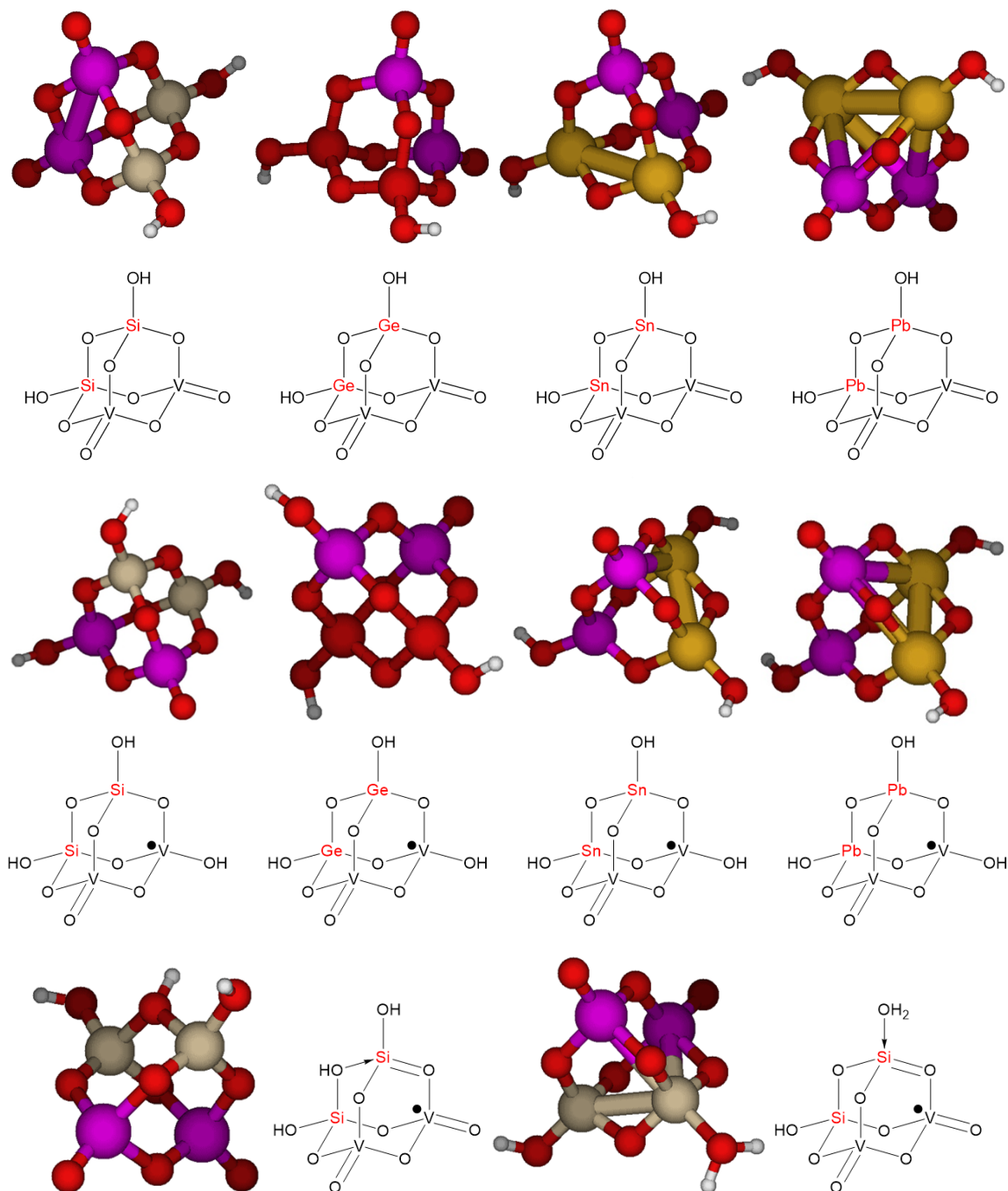
Figure 4.16. Optimized structures of the molybdenum-containing species $P_2Mo_2O_{11}$, $Te_2Mo_2O_{10}$, and $Te_2Mo_2O_{12}$ (first row), along with their schematic representations (second row); optimized structures of the corresponding monohydrogenated species (third row) and their schematic representations (fourth row). Mulliken spin density was used to assign radical character. All numbers are in kcal/mol.

D_H (P) = 81.3 D_H (Te^{IV}) = 67.7 D_H (Te^{VI}) = 86.3
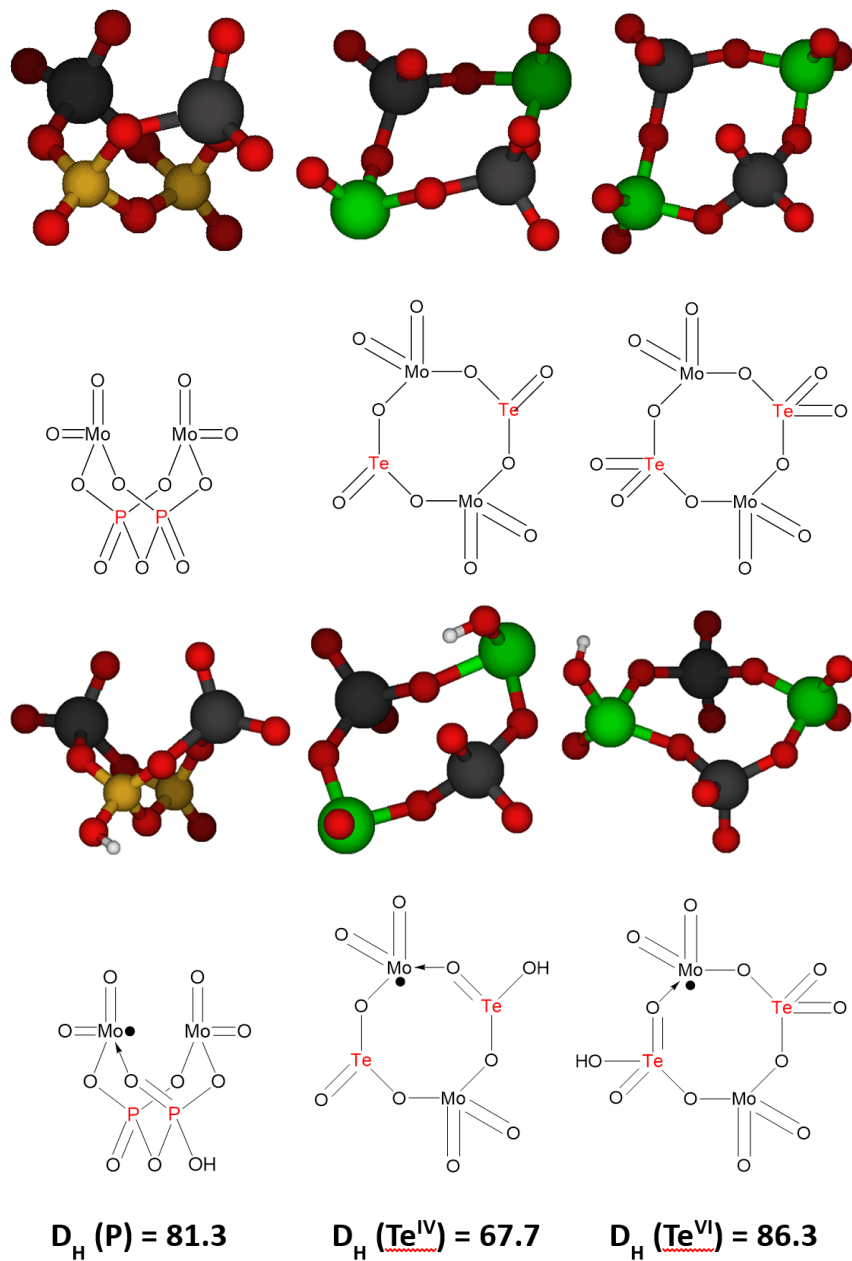
4.5 Reactions of a homogeneous oxidation catalyst utilizing the ROA mechanistic motif

Potential catalysts incorporating $\kappa-$P phosphinite coordination to metal, i.e. a direct V$-$P bond as in Figure 4.4b, were explored. Although the inspiration for our proposed catalyst structure was heuristic in nature, our confidence in its predicted activity is to a large degree bolstered by comprehensive theoretical investigations in the system using density functional theory. In this section we will discuss our results on various potential reactivity pathways, and suggest additional theoretical pathways that ought to be investigated before experimental work commences.

One potential pitfall in the installation of the bis(2-phenoxyl)phosphinite (OPO) ligand onto V would be the possibility of the P$=$O moiety on the ligand coordinating *via* the oxygen atom to the vanadium. However, at no time in our DFT geometry optimizations, aside from some high energy dianionic five-coordinate cases, did we see this sort of isomerization happen, nor did we see negative frequencies in our calculated Hessian matrices. This implies that the homogeneous vanadium complex with a V$-$P$=$O unit is a stable coordination isomer that may be realistically synthesized.

4.5.1 Nomenclature

Due to the number of complexes investigated, a systematic shorthand naming convention is desirable. As all of our complexes share the common motif of a vanadium atom bound $\kappa-$P to the O$-$P($=$O)$-$O pincer ligand bis(2-phenoxyl)phosphinite (OPO); we denote this commonality as (OPO)V. If there is an additional R group (such as a hydrogen atom) on the PO moiety of the (OPO), we label it as a subscript: $(\text{OPO})_{\text{R}}\text{V}$. If the V atom is five-coordinate, then there are two remaining coordination sites; these are labeled with the s or a superscripts depending on whether they are synperiplanar (*syn*) or antiperiplanar (*anti*) to the bis(2-phenoxyl)phosphinite's PO moiety, respectively (Figure 4.17, left). If the V atom is six-coordinate, then the (OPO) ligand may be in either a facial (*fac*) or meridional (*mer*) configuration (Figure 4.17, center and right, respectively); and there are three remaining coordination sites. In the *fac* case, the three sites are labeled with the c, s, and t superscripts, depending on whether they are clinal or *syn* to the PO moiety of the (OPO), or *trans* to the P, respectively. In the *mer* case, the three coordination sites are labeled with the s, t, or a superscripts, depending on whether they are *syn* to the PO, *trans* to the P, or *anti* to the PO, respectively. Under this system, the two specific conformational species shown in the right side of Figure 4.6 could be unambiguously expressed as $(\text{OPO})^f\text{V}^\text{V}\text{O}^s\text{L}_2^{ct}$ and $(\text{OPO})^m\text{V}^\text{V}\text{O}^s\text{L}_2^{ta}$.

Figure 4.17. Template for the nomenclature of investigated complexes. For the (OPO) ligand, an f super-script denotes that the chelation is facial whereas an m superscript denotes that it is meridional. For the V, n is the oxidation state. For the ligands L_n, the superscript a denotes that the ligand is *anti* to the PO moiety; s denotes that it is *syn* to the PO moiety; c denotes that it is *clinal* to the PO moiety; and t denotes that it is *trans* to the P atom.

$$(OPO)_R V^n (L_1)^s (L_2)^a \qquad (OPO)_R^f V^n (L_1)^c (L_2)^s (L_3)^t \qquad (OPO)_R^m V^n (L_1)^s (L_2)^t (L_3)^a$$
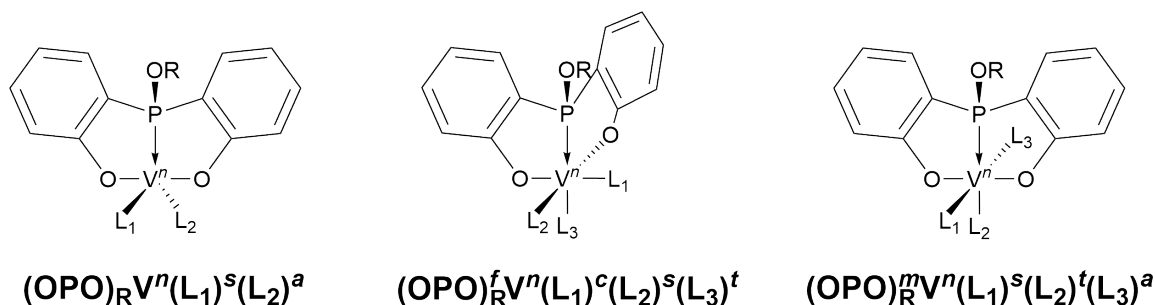
4.5.2 The resting V^V state

The first consideration that needs to be investigated is the precise nature of the resting V^V state: whether it is five or six coordinated, charged or uncharged, with the (OPO) ligand in a *fac* or *mer* conformation, and with what optimal combination of oxo, hydroxo, and aqua ligands. The pH of the environments investigated was set to either 0 or 7. Changing the ambient pH does not affect the relative energetics of isomeric species with the same charge, but does change which charge cohort of species will be most stable.

Table 4.1 is a comprehensive compilation of all $(OPO)V^V{=}O$ species studied. The most stable species at pH 0 is the neutral $(OPO)_H^f V^V O^c (OH)^s (H_2O)^t$, in which the P=O moiety on the ligand is already protonated. However, the isomer $(OPO)^f V^V O^c (H_2O)_2^{st}$, which does have a P=O moiety available, is the second-lowest energy species at only 1.6 kcal/mol higher. At pH 7, the most stable species is the doubly deprotonated $[(OPO)^f V^V O^c (OH)_2^{st}]^{2-}$. The optimized structures of these three species are shown in Figure 4.18. Note that in some *fac* cases, the PO moiety is twisted enough such that the clinal and *syn* positions on the V both become *gauche*. Since this phenomenon was not universal, no relabeling of clinal and *syn* markers was done.

Species	E_{gas}	G_{aq}	$G_{\text{rel}}(\text{pH}=0)$	$G_{\text{rel}}(\text{pH}=7)$
$(OPO)V^V{=}O$	-1481.9660	-1481.7587	20.9	29.8
$(OPO)V^V O^s (H_2O)^a$	-1711.4245	-1711.1621	2.8	11.7
$(OPO)V^V O^a (H_2O)^s$	-1711.4238	-1711.1506	10.0	18.9

Species	E_{gas}	G_{aq}	$G_{\text{rel}}(\text{pH}=0)$	$G_{\text{rel}}(\text{pH}=7)$
$(OPO)V^V(OH)_2$	-1711.4121	-1711.1479	8.6	20.5
$(OPO)_H V^V O^s(OH)^a$	geometry unstable			
$(OPO)_H V^V O^a(OH)^s$	geometry unstable			
$[(OPO)_H V^V O^s(H_2O)^a]^+$	-1711.8126	-1711.5923	3.1	21.5
$[(OPO)_H V^V O^a(H_2O)^s]^+$	geometry unstable			
$[(OPO)V^V O^s(OH)^a]^-$	-1710.9247	-1710.7246	7.0	6.4
$[(OPO)V^V O^a(OH)^s]^-$	-1710.9181	-1710.7148	13.1	12.5
$[(OPO)V^V O_2]^{2-}$	-1710.3205	-1710.2869	11.4	1.2
$(OPO)^f V^V O^c(H_2O)_2^{st}$	-1940.8700	-1940.5384	1.6	10.5
$(OPO)^f V^V O^s(H_2O)_2^{ct}$	-1940.8658	-1940.5334	4.8	13.7
$(OPO)^f V^V O^t(H_2O)_2^{cs}$	-1940.8678	-1940.5327	5.2	14.1
$(OPO)_H^f V^V O^c(OH)^s(H_2O)^t$	-1940.8696	-1940.5410	0.0	8.9
$(OPO)_H^f V^V O^c(OH)^t(H_2O)^s$	-1940.8648	-1940.5338	4.5	13.4
$(OPO)_H^f V^V O^s(OH)^c(H_2O)^t$	-1940.8690	-1940.5363	2.9	11.8
$(OPO)_H^f V^V O^s(OH)^t(H_2O)^c$	-1940.8598	-1940.5254	9.8	18.7
$(OPO)_H^f V^V O^t(OH)^c(H_2O)^s$	-1940.8744	-1940.5375	2.2	11.1
$(OPO)_H^f V^V O^t(OH)^s(H_2O)^c$	-1940.8719	-1940.5372	2.4	11.3
$[(OPO)_H^f V^V O^c(OH)_2^{st}]^-$	-1940.3696	-1940.0919	11.5	10.9
$[(OPO)_H^f V^V O^s(OH)_2^{ct}]^-$	-1940.3858	-1940.0992	6.9	6.3
$[(OPO)_H^f V^V O^t(OH)_2^{cs}]^-$	-1940.3795	-1940.0966	8.6	8.0
$[(OPO)^f V^V O^c(OH)^s(H_2O)^t]^-$	-1940.3743	-1940.0988	7.2	6.6
$[(OPO)^f V^V O^c(OH)^t(H_2O)^s]^-$	-1940.3722	-1940.0978	7.8	7.2
$[(OPO)^f V^V O^s(OH)^c(H_2O)^t]^-$	-1940.3677	-1940.0910	12.1	11.5

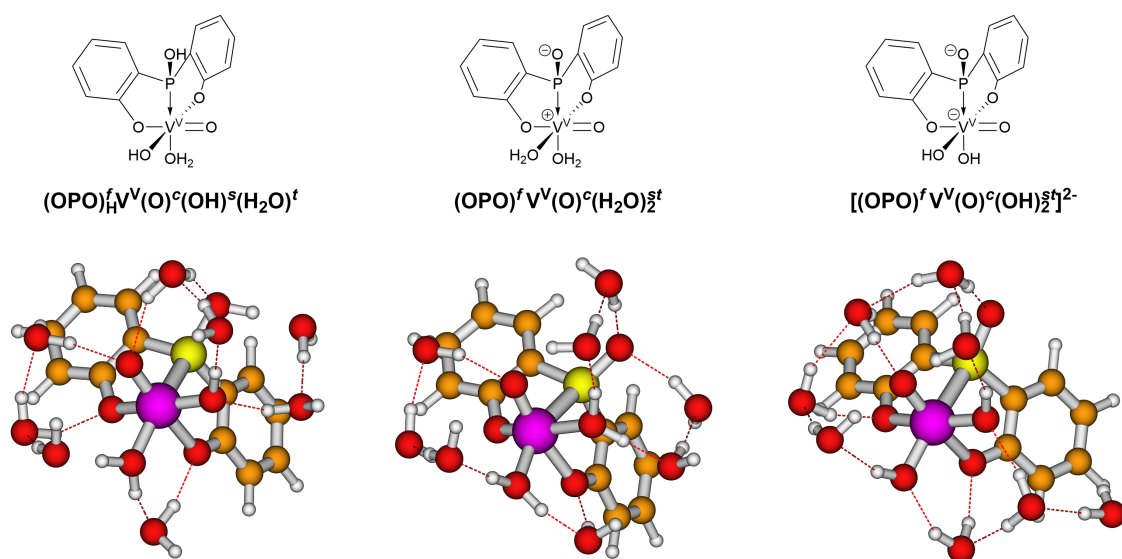| Species	E_{gas}	G_{aq}	$G_{\text{rel}}(\text{pH}=0)$	$G_{\text{rel}}(\text{pH}=7)$
$[(\text{OPO})^f\text{V}^\text{V}\text{O}^s(\text{OH})^t(\text{H}_2\text{O})^c]^-$	-1940.3600	-1940.0874	14.3	13.7
$[(\text{OPO})^f\text{V}^\text{V}\text{O}^t(\text{OH})^c(\text{H}_2\text{O})^s]^-$	-1940.3649	-1940.0887	13.5	12.9
$[(\text{OPO})^f\text{V}^\text{V}\text{O}^t(\text{OH})^s(\text{H}_2\text{O})^c]^-$	-1940.3726	-1940.0916	11.8	11.1
$[(\text{OPO})^f\text{V}^\text{V}\text{O}^c(\text{OH})_2^{st}]^{2-}$	-1939.7811	-1939.6634	10.1	0.0
$[(\text{OPO})^f\text{V}^\text{V}\text{O}^s(\text{OH})_2^{ct}]^{2-}$	-1939.7864	-1939.6622	10.9	0.7
$[(\text{OPO})^f\text{V}^\text{V}\text{O}^t(\text{OH})_2^{cs}]^{2-}$	-1939.7640	-1939.6517	17.5	7.3
$[(\text{OPO})^f\text{V}^\text{V}(\text{H}_2\text{O})^c(\text{O})_2^{st}]^{2-}$	-1939.7706	-1939.6550	15.4	5.3
$[(\text{OPO})^f\text{V}^\text{V}(\text{H}_2\text{O})^s(\text{O})_2^{ct}]^{2-}$	-1939.7651	-1939.6465	20.7	10.6
$[(\text{OPO})^f\text{V}^\text{V}(\text{H}_2\text{O})^t(\text{O})_2^{cs}]^{2-}$	-1939.7836	-1939.6595	12.6	2.4
$[(\text{OPO})_\text{H}^f\text{V}^\text{V}(\text{OH})^c(\text{O})_2^{st}]^{2-}$	-1939.7795	-1939.6556	15.0	4.9
$[(\text{OPO})_\text{H}^f\text{V}^\text{V}(\text{OH})^s(\text{O})_2^{ct}]^{2-}$	-1939.7662	-1939.6425	23.3	13.1
$[(\text{OPO})_\text{H}^f\text{V}^\text{V}(\text{OH})^t(\text{O})_2^{cs}]^{2-}$	-1939.7788	-1939.6546	15.7	5.5
$(\text{OPO})^m\text{V}^\text{V}\text{O}^s(\text{H}_2\text{O})_2^{ta}$	-1940.8672	-1940.5346	4.0	12.9
$(\text{OPO})^m\text{V}^\text{V}\text{O}^t(\text{H}_2\text{O})_2^{sa}$	-1940.8513	-1940.5180	14.5	23.4
$(\text{OPO})^m\text{V}^\text{V}\text{O}^a(\text{H}_2\text{O})_2^{st}$	-1940.8592	-1940.5289	7.6	16.5
$(\text{OPO})_\text{H}^m\text{V}^\text{V}\text{O}^s(\text{OH})^t(\text{H}_2\text{O})^a$	geometry unstable			
$(\text{OPO})_\text{H}^m\text{V}^\text{V}\text{O}^s(\text{OH})^a(\text{H}_2\text{O})^t$	geometry unstable			
$(\text{OPO})_\text{H}^m\text{V}^\text{V}\text{O}^t(\text{OH})^s(\text{H}_2\text{O})^a$	geometry unstable			
$(\text{OPO})_\text{H}^m\text{V}^\text{V}\text{O}^t(\text{OH})^a(\text{H}_2\text{O})^s$	-1940.8548	-1940.5201	13.1	22.0
$(\text{OPO})_\text{H}^m\text{V}^\text{V}\text{O}^a(\text{OH})^s(\text{H}_2\text{O})^t$	-1940.8449	-1940.5093	19.9	28.8
$(\text{OPO})_\text{H}^m\text{V}^\text{V}\text{O}^a(\text{OH})^t(\text{H}_2\text{O})^s$	-1940.8578	-1940.5270	8.8	17.7
$[(\text{OPO})^m\text{V}^\text{V}\text{O}^s(\text{OH})^t(\text{H}_2\text{O})^a]^-$	-1940.3660	-1940.0966	8.6	7.9
$[(\text{OPO})^m\text{V}^\text{V}\text{O}^s(\text{OH})^a(\text{H}_2\text{O})^t]^-$	geometry unstable			

Species	E_{gas}	G_{aq}	$G_{\text{rel}}(\text{pH}=0)$	$G_{\text{rel}}(\text{pH}=7)$
$[(OPO)^m V^V O^t (OH)^s (H_2O)^a]^-$	geometry unstable			
$[(OPO)^m V^V O^t (OH)^a (H_2O)^s]^-$	-1940.3614	-1940.0845	16.2	15.6
$[(OPO)^m V^V O^a (OH)^s (H_2O)^t]^-$	geometry unstable			
$[(OPO)^m V^V O^a (OH)^t (H_2O)^s]^-$	-1940.3724	-1940.0932	10.7	10.1
$[(OPO)_H^m V^V O^s (OH)_2^{ta}]^-$	-1940.3355	-1940.0626	29.9	29.3
$[(OPO)_H^m V^V O^t (OH)_2^{sa}]^-$	-1940.3573	-1940.0785	20.0	19.3
$[(OPO)_H^m V^V O^a (OH)_2^{st}]^-$	-1940.3447	-1940.0654	28.1	27.5
$[(OPO)^m V^V O^s (OH)_2^{ta}]^{2-}$	-1939.7563	-1939.6389	25.5	15.3
$[(OPO)^m V^V O^t (OH)_2^{sa}]^{2-}$	-1939.7430	-1939.6271	32.9	22.7
$[(OPO)^m V^V O^a (OH)_2^{st}]^{2-}$	-1939.7472	-1939.6324	29.6	19.4
$[(OPO)^m V^V (H_2O)^s (O)_2^{ta}]^{2-}$	geometry unstable			
$[(OPO)^m V^V (H_2O)^t (O)_2^{sa}]^{2-}$	geometry unstable			
$[(OPO)^m V^V (H_2O)^a (O)_2^{st}]^{2-}$	geometry unstable			
$[(OPO)_H^m V^V (OH)^s (O)_2^{ta}]^{2-}$	-1939.7499	-1939.6332	29.1	18.9
$[(OPO)_H^m V^V (OH)^t (O)_2^{sa}]^{2-}$	-1939.7799	-1939.6580	13.5	3.4
$[(OPO)_H^m V^V (OH)^a (O)_2^{st}]^{2-}$	-1939.7503	-1939.6286	32.0	21.8

Table 4.1. Comprehensive compilation of all $(OPO)V^V$ species studied, along with their gas-phase energies (E_{gas}) and aqueous free energies (G_{aq}), both in hartrees. The last two columns show their aqueous free energies relative to each other, in kcal/mol, at pH 0 and 7, respectively. For some entries, geometry optimization led to the formation of a lower-energy isomer. The energies for these entries are not reported.

4.5.3 Propane activation transition states

Propane consists of two types of C−H bonds: primary and secondary, and the secondary C−H bond in the middle carbon is more easily activated due to the increased stability of the resulting secondary radical. Those $(OPO)V^V$ species listed in Table 4.1 which contain unadorned intact P=O moieties were further investigated for their ability to activate the secondary C−H bond of propane. The transition states were located and their free energies at pH 0 and 7 relative to the ground $(OPO)V^V$ states of $(OPO)_H^f V^V O^c (OH)^s (H_2O)^t$ and $[(OPO)^f V^V O^c (OH)_2^{st}]^{2-}$, respectively, were calculated. The results are shown in Table 4.2.

Figure 4.18. The geometry-optimized structures of $(OPO)_H^f V^V O^c(OH)^s(H_2O)^t$ and $(OPO)^f V^V O^c(H_2O)_2^{st}$, the most stable $(OPO)V^V$ isomers at pH 0; and of the doubly deprotonated $[(OPO)^f V^V O^c(OH)_2^{st}]^{2-}$, the most stable isomer at pH 7.

$(OPO)_H^f V^V(O)^c(OH)^s(H_2O)^t$ $(OPO)^f V^V(O)^c(H_2O)_2^{st}$ $[(OPO)^f V^V(O)^c(OH)_2^{st}]^{2-}$

Species	E_{gas}	G_{aq}	$G_{\text{rel}}(\text{pH}=0)$	$G_{\text{rel}}(\text{pH}=7)$
$[(OPO)_{HiPr}V^V O^s(H_2O)^a]^{\ddagger}$	-1830.5749	-1830.2107	39.6	48.5
$[(OPO)_{HiPr}V^V O^a(H_2O)^s]^{\ddagger}$	-1830.5628	-1830.1985	47.2	56.1
$[(OPO)_{HiPr}V^V O^s(OH)^a]^{-\ddagger}$	geometry unstable			
$[(OPO)_{HiPr}V^V O^a(OH)^s]^{-\ddagger}$	geometry unstable			
$[(OPO)_{HiPr}V^V O_2^{sa}]^{2-\ddagger}$	geometry unstable			
$[(OPO)_{HiPr}^m V^V O^s(H_2O)_2^{ta}]^{\ddagger}$	-2060.0127	-2059.5889	37.2	46.1
$[(OPO)_{HiPr}^m V^V O^t(H_2O)_2^{sa}]^{\ddagger}$	-2060.0129	-2059.5909	36.0	44.9
$[(OPO)_{HiPr}^m V^V O^a(H_2O)_2^{st}]^{\ddagger}$	-2060.0036	-2059.5752	45.9	54.8
$[(OPO)_{HiPr}^m V^V O^s(OH)^t(H_2O)^a]^{-\ddagger}$	-2059.5055	-2059.1441	46.1	45.5
$[(OPO)_{HiPr}^m V^V O^s(OH)^a(H_2O)^t]^{-\ddagger}$	-2059.4829	-2059.1232	59.2	58.6

| Species	E_{gas}	G_{aq}	$G_{\text{rel}}(\text{pH}=0)$	$G_{\text{rel}}(\text{pH}=7)$
$[(\text{OPO})^m_{\text{HiPr}}\text{V}^{\text{V}}\text{O}^t(\text{OH})^s(\text{H}_2\text{O})^a]^{-\ddagger}$	-2059.4979	-2059.1286	55.8	55.2
$[(\text{OPO})^m_{\text{HiPr}}\text{V}^{\text{V}}\text{O}^t(\text{OH})^a(\text{H}_2\text{O})^s]^{-\ddagger}$	-2059.5033	-2059.1384	49.7	49.1
$[(\text{OPO})^m_{\text{HiPr}}\text{V}^{\text{V}}\text{O}^a(\text{OH})^s(\text{H}_2\text{O})^t]^{-\ddagger}$	-2059.4868	-2059.1247	58.3	57.7
$[(\text{OPO})^m_{\text{HiPr}}\text{V}^{\text{V}}\text{O}^a(\text{OH})^t(\text{H}_2\text{O})^s]^{-\ddagger}$	-2059.4888	-2059.1282	56.1	55.4
$[(\text{OPO})^m_{\text{HiPr}}\text{V}^{\text{V}}\text{O}^s(\text{OH})_2^{ta}]^{2-\ddagger}$	-2058.9071	-2058.6901	60.7	50.6
$[(\text{OPO})^m_{\text{HiPr}}\text{V}^{\text{V}}\text{O}^t(\text{OH})_2^{sa}]^{2-\ddagger}$	-2058.8825	-2058.6799	67.1	57.0
$[(\text{OPO})^m_{\text{HiPr}}\text{V}^{\text{V}}\text{O}^a(\text{OH})_2^{st}]^{2-\ddagger}$	-2058.8811	-2058.6783	68.1	57.9
$[(\text{OPO})^m_{\text{HiPr}}\text{V}^{\text{V}}(\text{H}_2\text{O})^s\text{O}_2^{ta}]^{2-\ddagger}$	-2058.8702	-2058.6684	74.4	64.2
$[(\text{OPO})^m_{\text{HiPr}}\text{V}^{\text{V}}(\text{H}_2\text{O})^t\text{O}_2^{sa}]^{2-\ddagger}$	geometry unstable			
$[(\text{OPO})^m_{\text{HiPr}}\text{V}^{\text{V}}(\text{H}_2\text{O})^a\text{O}_2^{st}]^{2-\ddagger}$	geometry unstable			
$[(\text{OPO})^f_{\text{HiPr}}\text{V}^{\text{V}}\text{O}^c(\text{H}_2\text{O})_2^{st}]^{\ddagger}$	-2060.0212	-2059.6000	30.3	39.2
$[(\text{OPO})^f_{\text{HiPr}}\text{V}^{\text{V}}\text{O}^s(\text{H}_2\text{O})_2^{ct}]^{\ddagger}$	-2060.0208	-2059.5954	33.2	42.1
$[(\text{OPO})^f_{\text{HiPr}}\text{V}^{\text{V}}\text{O}^t(\text{H}_2\text{O})_2^{cs}]^{\ddagger}$	-2060.0229	-2059.5991	30.8	39.7
$[(\text{OPO})^f_{\text{HiPr}}\text{V}^{\text{V}}\text{O}^c(\text{OH})^s(\text{H}_2\text{O})^t]^{-\ddagger}$	-2059.5101	-2059.1478	43.8	43.1
$[(\text{OPO})^f_{\text{HiPr}}\text{V}^{\text{V}}\text{O}^c(\text{OH})^t(\text{H}_2\text{O})^s]^{-\ddagger}$	-2059.5120	-2059.1514	41.5	40.9
$[(\text{OPO})^f_{\text{HiPr}}\text{V}^{\text{V}}\text{O}^s(\text{OH})^c(\text{H}_2\text{O})^t]^{-\ddagger}$	-2059.5096	-2059.1432	46.7	46.1
$[(\text{OPO})^f_{\text{HiPr}}\text{V}^{\text{V}}\text{O}^s(\text{OH})^t(\text{H}_2\text{O})^c]^{-\ddagger}$	-2059.5118	-2059.1455	45.2	44.6
$[(\text{OPO})^f_{\text{HiPr}}\text{V}^{\text{V}}\text{O}^t(\text{OH})^c(\text{H}_2\text{O})^s]^{-\ddagger}$	-2059.5186	-2059.1506	42.0	41.4
$[(\text{OPO})^f_{\text{HiPr}}\text{V}^{\text{V}}\text{O}^t(\text{OH})^s(\text{H}_2\text{O})^c]^{-\ddagger}$	-2059.5170	-2059.1512	41.6	41.0
$[(\text{OPO})^f_{\text{HiPr}}\text{V}^{\text{V}}\text{O}^c(\text{OH})_2^{st}]^{2-\ddagger}$	-2058.9002	-2058.6969	56.4	46.3
$[(\text{OPO})^f_{\text{HiPr}}\text{V}^{\text{V}}\text{O}^s(\text{OH})_2^{ct}]^{2-\ddagger}$	-2058.9152	-2058.7010	53.9	43.7
$[(\text{OPO})^f_{\text{HiPr}}\text{V}^{\text{V}}\text{O}^t(\text{OH})_2^{cs}]^{2-\ddagger}$	-2058.9121	-2058.6971	56.3	46.2
$[(\text{OPO})^f_{\text{HiPr}}\text{V}^{\text{V}}(\text{H}_2\text{O})^c\text{O}_2^{st}]^{2-\ddagger}$	-2058.8851	-2058.6791	67.6	57.4

Species	E_{gas}	G_{aq}	$G_{\text{rel}}(\text{pH}=0)$	$G_{\text{rel}}(\text{pH}=7)$
$[(\text{OPO})^f_{\text{H}i\text{Pr}}\text{V}^{\text{V}}(\text{H}_2\text{O})^s\text{O}^{ct}_2]^{2-\ddagger}$	-2058.8771	-2058.6841	64.5	54.4
$[(\text{OPO})^f_{\text{H}i\text{Pr}}\text{V}^{\text{V}}(\text{H}_2\text{O})^t\text{O}^{cs}_2]^{2-\ddagger}$	-2058.8941	-2058.6763	69.4	59.3

Table 4.2. Comprehensive compilation of all the transition states for propane activation by $(\text{OPO})\text{V}^{\text{V}}$, along with their gas-phase energies (E_{gas}) and aqueous free energies (G_{aq}), both in hartrees. The last two columns show their aqueous free energies, in kcal/mol, relative to the ground states at pH 0 and 7 ($(\text{OPO})^f_{\text{H}}\text{V}^{\text{V}}\text{O}^c(\text{OH})^s(\text{H}_2\text{O})^t$ and $[(\text{OPO})^f\text{V}^{\text{V}}\text{O}^c(\text{OH})^{st}_2]^{2-}$, respectively). For some entries, geometry optimization led to the formation of a lower-energy isomer. The energies for these entries are not reported.

According to Table 4.2, the most favorable transition state at both pH 0 and 7 is the neutral species $[(\text{OPO})^f_{\text{H}i\text{Pr}}\text{V}^{\text{V}}\text{O}^c(\text{H}_2\text{O})^{st}_2]^{\ddagger}$, whose structure is shown in detail in Figure 4.19. At pH 0, this species is 30.3 kcal/mol above the neutral ground state $(\text{OPO})^f_{\text{H}}\text{V}^{\text{V}}\text{O}^c(\text{OH})^s(\text{H}_2\text{O})^t$, and with $\Delta G^{\ddagger} = 28.7$ kcal/mol from its immediate precursor $(\text{OPO})^f\text{V}^{\text{V}}\text{O}^c(\text{H}_2\text{O})^{st}_2$; we therefore consider it to be accessible for C−H activation. At pH 7, however, the species is 39.2 kcal/mol above the ground state $[(\text{OPO})^f\text{V}^{\text{V}}\text{O}^c(\text{OH})^{st}_2]^{2-}$, as this ground state must be the doubly protonated before C−H activation can occur. Doubly protonating the ground state before C−H activation is still preferable to the dianion directly activating propane; this is due to the fact that the negative charge stabilizes the $\text{V}^{\text{V}}{=}\text{O}$ moiety and thus decreases its tendency to be reduced to V^{IV}. We conclude from these results that catalysis with the $(\text{OPO})\text{V}$ system is much more likely at pH 0. Analysis of the Mulliken spin density supports our assignment of radical character: Whereas the overall spin is 0, the spin density on the vanadium (1.0882), propane's secondary carbon (-0.5389), and the attacking PO oxygen (-0.2084), but not the phosphorus itself (-0.0350), supporting our assertion of attack by the ROA mechanism.

Figure 4.19. The geometry-optimized structure of $[(\text{OPO})^f_{\text{H}i\text{Pr}}\text{V}^{\text{V}}\text{O}^c(\text{H}_2\text{O})^{st}_2]^{\ddagger}$, the most stable transition state for C−H activation of propane at either pH 0 or 7.
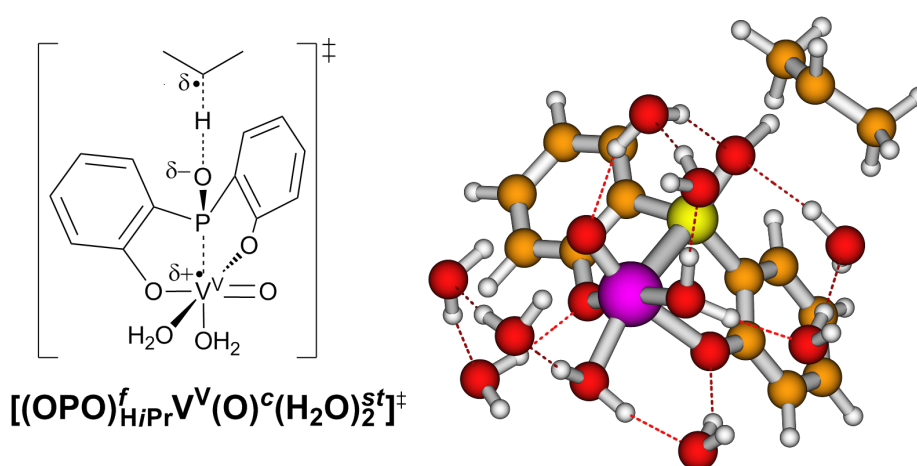
4.5.4 Monohydrogenated V^{IV} states

The result of the C−H activation transition states as described in the previous subsection is an iso-propyl radical and a monohydrogenated $(OPO)_H V^{IV}$ complex, which may then isomerize into other $(OPO)V^{IV}$ species. The various $(OPO)V^{IV}$ complexes are listed in Table 4.3. Only six-coordinate complexes with *fac*-(OPO) were exhaustively investigated, as Table 4.1 shows that they are lower in energy than their five-coordinate and six-coordinate *mer* counterparts. At pH 0, the lowest energy species is $(OPO)_H^f V^{IV} O^c (H_2O)_2^{st}$ at 13.4 kcal/mol above the ground state. However, isomerization to $(OPO)^f V^{IV} (OH)^c (H_2O)_2^{st}$, at 13.6 kcal/mol above the ground state, is nearly thermoneutral. At pH 7, the lowest energy species is $[(OPO)^f V^{IV} O^s (H_2O)_2^{ct}]^-$ at 16.8 kcal/mol above the ground state. These species are shown in detail in Figure 4.20. All species are doublets, and Mulliken spin density analysis reveals that the spins are localized on the vanadium atoms, hence supporting the assignment of V in the +IV oxidation state.

Figure 4.20. The geometry-optimized structures of $(OPO)_H^f V^{IV} O^c (H_2O)_2^{st}$ and $(OPO)^f V^{IV} (OH)^c (H_2O)_2^{st}$, the most stable $(OPO)V^{IV}$ isomers at pH 0; and of the deprotonated $[(OPO)^f V^{IV} O^s (H_2O)_2^{ct}]^-$, the most stable isomer at pH 7.

(OPO)$_H^f$V^{IV}(O)^c(H$_2$O)$_2^{st}$ **(OPO)^f V^{IV}(OH)^c(H$_2$O)$_2^{st}$**   **[(OPO)^f V^{IV}(O)^s(H$_2$O)$_2^{ct}$]$^-$**
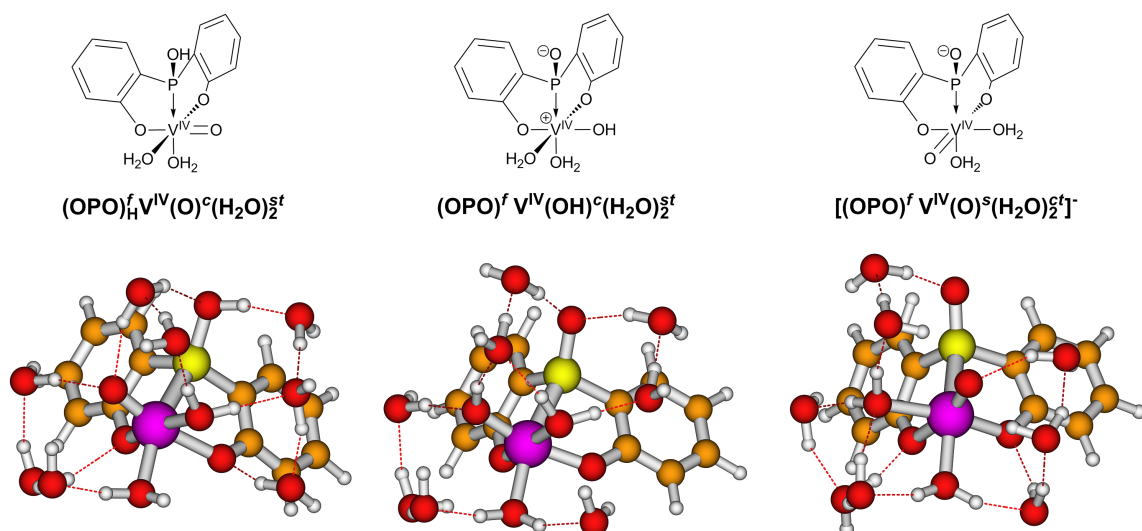
4.5.5 Catalytic cycle involving H-atom abstraction only

The simplest catalytic cycle that can now be envisioned is one that alternates only between the resting state and its corresponding monohydrogenated species, e.g., $(OPO)_H^f V^V O^c (OH)^s (H_2O)^t$ and $(OPO)_H^f V^{IV} O^c (H_2O)_2^{st}$ (We will only consider the pH 0 case since it is kinetically feasible with overall $\Delta G^\ddagger = 30.3$ kcal/mol; see Subsection 4.5.3). After monohydrogenation, the starting V^V species is regenerated by sequential removal of H^+ and e^- (Scheme 4.2). First deprotonating the

Species	E_{gas}	G_{aq}	$G_{\mathrm{rel}}(\mathrm{pH}=0)$	$G_{\mathrm{rel}}(\mathrm{pH}=7)$
$(OPO)_H V^{IV}(O)^s(H_2O)^a$	−1712.0701	−1711.7906	16.2	25.1
$(OPO)_H V^{IV}(O)^a(H_2O)^s$	−1712.0474	−1711.7653	32.1	41.0
$[(OPO)V^{IV}(O)^s(H_2O)^a]^-$	−1711.5717	−1711.3486	23.3	22.7
$[(OPO)V^{IV}(O)^a(H_2O)^s]^-$	−1711.5440	−1711.3323	33.5	32.9
$(OPO)_H^m V^{IV}(O)^s(H_2O)_2^{ta}$	−1941.5038	−1941.1599	19.5	28.4
$(OPO)_H^m V^{IV}(O)^t(H_2O)_2^{sa}$	−1941.4939	−1941.1627	17.7	26.6
$(OPO)_H^m V^{IV}(O)^a(H_2O)_2^{st}$	−1941.4894	−1941.1451	28.8	37.7
$[(OPO)^m V^{IV}(O)^s(H_2O)_2^{ta}]^-$	−1940.9974	−1940.7170	27.1	26.5
$[(OPO)^m V^{IV}(O)^t(H_2O)_2^{sa}]^-$	−1940.9955	−1940.7103	31.3	30.7
$[(OPO)^m V^{IV}(O)^a(H_2O)_2^{st}]^-$	−1941.0011	−1940.7064	33.8	33.1
$(OPO)^f V^{IV}(OH)^c(H_2O)_2^{st}$	−1941.5108	−1941.1692	13.6	22.5
$(OPO)^f V^{IV}(OH)^s(H_2O)_2^{ct}$	−1941.5065	−1941.1636	17.2	26.1
$(OPO)^f V^{IV}(OH)^t(H_2O)_2^{cs}$	−1941.4999	−1941.1580	20.7	29.6
$(OPO)_H^f V^{IV}(H_2O)^c(OH)_2^{st}$	−1941.4953	−1941.1503	25.5	34.4
$(OPO)_H^f V^{IV}(H_2O)^s(OH)_2^{ct}$	−1941.4931	−1941.1497	25.9	34.7
$(OPO)_H^f V^{IV}(H_2O)^t(OH)_2^{cs}$	−1941.5068	−1941.1598	19.5	28.4
$(OPO)_H^f V^{IV}(O)^c(H_2O)_2^{st}$	−1941.5092	−1941.1695	13.4	22.3
$(OPO)_H^f V^{IV}(O)^s(H_2O)_2^{ct}$	−1941.5180	−1941.1663	15.4	24.3
$(OPO)_H^f V^{IV}(O)^t(H_2O)_2^{cs}$	−1941.5093	−1941.1667	15.2	24.1
$[(OPO)^f V^{IV}(O)^c(H_2O)_2^{st}]^-$	−1941.0201	−1940.7264	21.2	20.6
$[(OPO)^f V^{IV}(O)^s(H_2O)_2^{ct}]^-$	−1941.0201	−1940.7325	17.4	16.8
$[(OPO)^f V^{IV}(O)^t(H_2O)_2^{cs}]^-$	−1941.0125	−1940.7266	21.1	20.5
$[(OPO)_H^f V^{IV}(O)^c(OH)^s(H_2O)^t]^-$	−1940.9999	−1940.7101	31.4	30.8
$[(OPO)_H^f V^{IV}(O)^c(OH)^t(H_2O)^s]^-$	−1941.0011	−1940.7205	24.9	24.3
$[(OPO)_H^f V^{IV}(O)^s(OH)^c(H_2O)^t]^-$	−1941.0136	−1940.7218	24.1	23.5
$[(OPO)_H^f V^{IV}(O)^s(OH)^t(H_2O)^c]^-$	−1941.0143	−1940.7228	23.5	22.9
$[(OPO)_H^f V^{IV}(O)^t(OH)^c(H_2O)^s]^-$	−1941.0161	−1940.7247	22.3	21.6
$[(OPO)_H^f V^{IV}(O)^t(OH)^s(H_2O)^c]^-$	−1941.0095	−1940.7226	23.6	23.0
$[(OPO)^f V^{IV}(O)^c(OH)^s(H_2O)^t]^{2-}$	−1940.4101	−1940.2769	33.0	22.8
$[(OPO)^f V^{IV}(O)^c(OH)^t(H_2O)^s]^{2-}$	−1940.4110	−1940.2804	30.8	20.6
$[(OPO)^f V^{IV}(O)^s(OH)^c(H_2O)^t]^{2-}$	−1940.4079	−1940.2745	34.5	24.4
$[(OPO)^f V^{IV}(O)^s(OH)^t(H_2O)^c]^{2-}$	−1940.4018	−1940.2721	36.0	25.8
$[(OPO)^f V^{IV}(O)^t(OH)^c(H_2O)^s]^{2-}$	−1940.4013	−1940.2790	31.7	21.5
$[(OPO)^f V^{IV}(O)^t(OH)^s(H_2O)^c]^{2-}$	−1940.3952	−1940.2736	35.1	24.9
$[(OPO)_H^f V^{IV}(O)^c(OH)_2^{st}]^{2-}$	−1940.3899	−1940.2599	43.6	33.5
$[(OPO)_H^f V^{IV}(O)^s(OH)_2^{st}]^{2-}$	−1940.4093	−1940.2757	33.8	23.6
$[(OPO)_H^f V^{IV}(O)^t(OH)_2^{st}]^{2-}$	−1940.4031	−1940.2828	29.3	19.2

Table 4.3. Comprehensive compilation of all $(OPO)V^{IV}$ species studied, along with their gas-phase energies (E_{gas}) and aqueous free energies (G_{aq}), both in hartrees. The last two columns show their aqueous free energies, in kcal/mol, relative to the ground states at pH 0 and 7 ($(OPO)_H^f V^V O^c(OH)^s(H_2O)^t$ and $[(OPO)^f V^V O^c(OH)_2^{st}]^{2-}$, respectively).

monohydrogenated $(OPO)_H^f V^{IV} O^c (H_2O)_2^{st}$ forms the anionic intermediates $[(OPO)V^{IV}O(H_2O)_2]^-$, the lowest isomer of which $([(OPO)^f V^{IV}(O)^s (H_2O)_2^{ct}]^-)$ is 17.4 kcal/mol above the starting complex. The deprotonation energy gain of 4.0 kcal/mol leads to a calculated pK_a value of 2.9 for the neutral monohydrogenated complex $(OPO)_H^f V^{IV} O^c (H_2O)_2^{st}$. However, the reduction potential of the neutral $(OPO)^f V^V O^s (H_2O)_2^{ct}$ is calculated to be 1.07 V versus SHE, whereas that of $(OPO)^f V^V O^c (H_2O)_2^{st}$ is calculated to be 0.77 V versus SHE. Hence, it is difficult to reoxidize the deprotonated $[(OPO)^f V^{IV} O^c$-$(H_2O)_2^{st}]^-$ back to V^V, but not impossible; since the standard reduction potential of O_2 is 1.23 V $vs.$ SHE.

Scheme 4.2. Potential catalytic cycle involving H-atom abstraction only: The one-electron oxidation and catalyst regeneration that forms the core of this catalytic cycle. All energies are in kcal/mol. Note that the overall reaction in this cycle is $C_3H_8 + \frac{1}{2}O_2 \longrightarrow C_3H_6 + H_2O$, with $\Delta G = -32.3$ kcal/mol. Hence, whereas the $(OPO)^f V^V O^c (H_2O)_2^{st}$ and $(OPO)^f V^V O^s (H_2O)_2^{ct}$ complexes are initially 1.6 and 4.8 kcal/mol above the starting state, after one complete cycle they are -30.7 and -27.4 kcal/mol below the starting state, respectively.

Since this would only be a one-electron oxidative process, two complete cycles are necessary for propane oxidation: first to abstract a hydrogen atom from the starting alkane, and then to abstract a second hydrogen atom from the resulting isopropyl radical. As hydrogen abstraction from an alkyl radical to a closed-shell species is expected to be facile, the rate-limiting step in this case will be the initial propane activation step. From the $(OPO)^f V^V O^c (H_2O)_2^{st}$ precursor (1.6 kcal/mol above the ground state), initial H-atom abstraction from propane is uphill by 11.8 kcal/mol. As the weakest C$-$H bond in propane (i.e. the iPr$-$H bond) has a dissociation energy of 103 kcal, this implies a very strong hydrogen abstracting power of 91.2 kcal/mol. This number is very close to the hydrogen-abstraction power of the P=O moiety in $V^V OPO_4$, the oxidized surface of the VPO catalyst [3], hence confirming the validity of our ROA mechanism as modified in Figure 4.4b. The overall kinetic

barrier for H-atom abstraction is 30.3 kcal/mol, a value that is low enough to be accessible at elevated reaction temperatures.

As indicated by Scheme 4.2 and its associated discussion, deprotonation of the monohydrogenated $(OPO)_H^f V^{IV} O^c (H_2O)_2^{st}$ precedes oxidation back to a V^V species. In fact, these steps are both slightly uphill, by 4.0 and 1.6 kcal/mol, respectively, but they are low enough to remain feasible. The second H-atom abstraction, from the isopropyl radical, is quite facile as expected, creating propylene as the oxidation product. The resulting $(OPO)_H^f V^{IV} O^c (H_2O)_2^{st}$ then goes through one more deprotonation, oxidation, and isomerization cycle to regenerate the starting catalyst. Overall, this reaction is quite feasible thermodynamically, and the reaction barriers are not expected to be large, either. Hence we can expect this to be a complete potential catalytic cycle for the dehydrogenation of propane to propylene.

4.5.6 Reduced V^{III} states

Since reactive isopropyl radicals are generated upon H-atom abstraction, it is necessary to also consider the possibility that they may be trapped by the V^{IV} intermediate instead of being converted to propylene by another equivalent of a V^V species. Once again taking inspiration from Cheng and Goddard [3], in which the produced isopropyl radical is adsorbed onto a V=O moiety, we analogously considered the possibility that the isopropyl radical and monohydrogenated $(OPO)V^{IV}(O)(H_2O)_2$ species react with each other to form $(OPO)V^{III}(OiPr)$ species. The isopropoxy ligand may then be protonated and exchanged with an aqua ligand, resulting in isopropanol being produced.

Table 4.4 is a comprehensive list of $(OPO)V^{III}$ species with only oxo/hydroxo/aqua ligands, and neutral or -1 charge. As in the case of the V^V and V^{IV} species, the $(OPO)V^{III}$ species are most stable with the (OPO) ligand in the *fac* configuration. Furthermore, the triplet states are universally more stable than their singlet counterparts, supporting the $+III$ assignment for the vanadium atom's oxidation state. Hence, Table 4.5, which lists the $(OPO)V^{III}(OiPr)$ species, only contains the triplet six coordinate species with the (OPO) ligand in the *fac* configuration.

Species	E_{gas}	G_{aq}	$G_{\text{rel}}(\text{pH}=0)$	$G_{\text{rel}}(\text{pH}=7)$
$^1(OPO)V^{III}(H_2O)_2^{sa}$	-1712.6358	-1712.3473	25.0	33.9
$^3(OPO)V^{III}(H_2O)_2^{sa}$	-1712.6811	-1712.3911	-2.5	6.4
$^1(OPO)_H V^{III}(OH)^s(H_2O)^a$	geometry unstable			
$^3(OPO)_H V^{III}(OH)^s(H_2O)^a$	-1712.6895	-1712.3998	-7.9	1.0

Species	E_{gas}	G_{aq}	$G_{\text{rel}}(\text{pH}=0)$	$G_{\text{rel}}(\text{pH}=7)$
$^1(\text{OPO})_{\text{H}}\text{V}^{\text{III}}(\text{OH})^a(\text{H}_2\text{O})^s$	-1712.6609	-1712.3705	10.5	19.4
$^3(\text{OPO})_{\text{H}}\text{V}^{\text{III}}(\text{OH})^a(\text{H}_2\text{O})^s$	-1712.6784	-1712.3916	-2.7	6.2
$^1[(\text{OPO})\text{V}^{\text{III}}(\text{OH})^s(\text{H}_2\text{O})^a]^-$	geometry unstable			
$^3[(\text{OPO})\text{V}^{\text{III}}(\text{OH})^s(\text{H}_2\text{O})^a]^-$	-1712.1787	-1711.9442	7.7	7.1
$^1[(\text{OPO})\text{V}^{\text{III}}(\text{OH})^a(\text{H}_2\text{O})^s]^-$	geometry unstable			
$^3[(\text{OPO})\text{V}^{\text{III}}(\text{OH})^a(\text{H}_2\text{O})^s]^-$	-1712.1727	-1711.9391	10.9	10.3
$^1[(\text{OPO})_{\text{H}}\text{V}^{\text{III}}(\text{OH})_2^{sa}]^-$	geometry unstable			
$^3[(\text{OPO})_{\text{H}}\text{V}^{\text{III}}(\text{OH})_2^{sa}]^-$	geometry unstable			
$^1(\text{OPO})^m\text{V}^{\text{III}}(\text{H}_2\text{O})_3^{sta}$	-1942.0707	-1941.7179	27.5	36.4
$^3(\text{OPO})^m\text{V}^{\text{III}}(\text{H}_2\text{O})_3^{sta}$	-1942.1201	-1941.7641	-1.5	7.4
$^1(\text{OPO})_{\text{H}}^m\text{V}^{\text{III}}(\text{OH})^s(\text{H}_2\text{O})_2^{ta}$	-1942.0625	-1941.7111	31.8	40.7
$^3(\text{OPO})_{\text{H}}^m\text{V}^{\text{III}}(\text{OH})^s(\text{H}_2\text{O})_2^{ta}$	-1942.1196	-1941.7628	-0.7	8.2
$^1(\text{OPO})_{\text{H}}^m\text{V}^{\text{III}}(\text{OH})^t(\text{H}_2\text{O})_2^{sa}$	-1942.0710	-1941.7216	25.2	34.1
$^3(\text{OPO})_{\text{H}}^m\text{V}^{\text{III}}(\text{OH})^t(\text{H}_2\text{O})_2^{sa}$	-1942.1162	-1941.7627	-0.6	8.3
$^1(\text{OPO})_{\text{H}}^m\text{V}^{\text{III}}(\text{OH})^a(\text{H}_2\text{O})_2^{st}$	-1942.0597	-1941.6995	39.1	48.0
$^3(\text{OPO})_{\text{H}}^m\text{V}^{\text{III}}(\text{OH})^a(\text{H}_2\text{O})_2^{st}$	-1942.1097	-1941.7567	3.2	12.0
$^1[(\text{OPO})^m\text{V}^{\text{III}}(\text{OH})^s(\text{H}_2\text{O})_2^{ta}]^-$	-1941.5661	-1941.2673	40.0	39.3
$^3[(\text{OPO})^m\text{V}^{\text{III}}(\text{OH})^s(\text{H}_2\text{O})_2^{ta}]^-$	-1941.6145	-1941.3211	6.2	5.6
$^1[(\text{OPO})^m\text{V}^{\text{III}}(\text{OH})^t(\text{H}_2\text{O})_2^{sa}]^-$	-1941.5611	-1941.2660	40.8	40.2
$^3[(\text{OPO})^m\text{V}^{\text{III}}(\text{OH})^t(\text{H}_2\text{O})_2^{sa}]^-$	-1941.6143	-1941.3217	5.8	5.2
$^1[(\text{OPO})^m\text{V}^{\text{III}}(\text{OH})^a(\text{H}_2\text{O})_2^{st}]^-$	-1941.5539	-1941.2535	48.6	48.0
$^3[(\text{OPO})^m\text{V}^{\text{III}}(\text{OH})^a(\text{H}_2\text{O})_2^{st}]^-$	-1941.6047	-1941.3114	12.3	11.7
$^1[(\text{OPO})_{\text{H}}^m\text{V}^{\text{III}}(\text{H}_2\text{O})^s(\text{OH})_2^{ta}]^-$	-1941.5762	-1941.2783	33.1	32.5

Species	E_{gas}	G_{aq}	$G_{\text{rel}}(\text{pH}=0)$	$G_{\text{rel}}(\text{pH}=7)$
$^3[(\text{OPO})_{\text{H}}^m\text{V}^{\text{III}}(\text{H}_2\text{O})^s(\text{OH})_2^{ta}]^-$	-1941.5886	-1941.3002	19.3	18.7
$^1[(\text{OPO})_{\text{H}}^m\text{V}^{\text{III}}(\text{H}_2\text{O})^t(\text{OH})_2^{sa}]^-$	-1941.5562	-1941.2561	47.0	46.4
$^3[(\text{OPO})_{\text{H}}^m\text{V}^{\text{III}}(\text{H}_2\text{O})^t(\text{OH})_2^{sa}]^-$	-1941.6073	-1941.3093	13.6	13.0
$^1[(\text{OPO})_{\text{H}}^m\text{V}^{\text{III}}(\text{H}_2\text{O})^a(\text{OH})_2^{st}]^-$	-1941.5988	-1941.3017	18.4	17.7
$^3[(\text{OPO})_{\text{H}}^m\text{V}^{\text{III}}(\text{H}_2\text{O})^a(\text{OH})_2^{st}]^-$	-1941.6188	-1941.3235	4.7	4.1
$^1(\text{OPO})^f\text{V}^{\text{III}}(\text{H}_2\text{O})_3^{cst}$	-1942.0823	-1941.7202	26.0	34.9
$^3(\text{OPO})^f\text{V}^{\text{III}}(\text{H}_2\text{O})_3^{cst}$	-1942.1432	-1941.7900	-17.7	-8.8
$^1(\text{OPO})_{\text{H}}^f\text{V}^{\text{III}}(\text{OH})^c(\text{H}_2\text{O})_2^{st}$	-1942.0873	-1941.7262	22.3	31.2
$^3(\text{OPO})_{\text{H}}^f\text{V}^{\text{III}}(\text{OH})^c(\text{H}_2\text{O})_2^{st}$	-1942.1429	-1941.7811	-12.2	-3.3
$^1(\text{OPO})_{\text{H}}^f\text{V}^{\text{III}}(\text{OH})^s(\text{H}_2\text{O})_2^{ct}$	-1942.0885	-1941.7307	19.5	28.4
$^3(\text{OPO})_{\text{H}}^f\text{V}^{\text{III}}(\text{OH})^s(\text{H}_2\text{O})_2^{ct}$	-1942.1386	-1941.7818	-12.6	-3.7
$^1(\text{OPO})_{\text{H}}^f\text{V}^{\text{III}}(\text{OH})^t(\text{H}_2\text{O})_2^{cs}$	-1942.0732	-1941.7139	30.0	38.9
$^3(\text{OPO})_{\text{H}}^f\text{V}^{\text{III}}(\text{OH})^t(\text{H}_2\text{O})_2^{cs}$	-1942.1288	-1941.7765	-9.3	-0.4
$^1[(\text{OPO})^f\text{V}^{\text{III}}(\text{OH})^c(\text{H}_2\text{O})_2^{st}]^-$	-1941.5871	-1941.2738	35.9	35.3
$^3[(\text{OPO})^f\text{V}^{\text{III}}(\text{OH})^c(\text{H}_2\text{O})_2^{st}]^-$	-1941.6398	-1941.3377	-4.2	-4.8
$^1[(\text{OPO})^f\text{V}^{\text{III}}(\text{OH})^s(\text{H}_2\text{O})_2^{ct}]^-$	-1941.5861	-1941.2299	63.4	62.8
$^3[(\text{OPO})^f\text{V}^{\text{III}}(\text{OH})^s(\text{H}_2\text{O})_2^{ct}]^-$	-1941.6343	-1941.3371	-3.8	-4.5
$^1[(\text{OPO})^f\text{V}^{\text{III}}(\text{OH})^t(\text{H}_2\text{O})_2^{cs}]^-$	-1941.5637	-1941.2725	36.7	36.1
$^3[(\text{OPO})^f\text{V}^{\text{III}}(\text{OH})^t(\text{H}_2\text{O})_2^{cs}]^-$	-1941.6283	-1941.3282	1.8	1.2
$^1[(\text{OPO})_{\text{H}}^f\text{V}^{\text{III}}(\text{H}_2\text{O})^c(\text{OH})_2^{st}]^-$	-1941.6034	-1941.3092	13.7	13.1
$^3[(\text{OPO})_{\text{H}}^f\text{V}^{\text{III}}(\text{H}_2\text{O})^c(\text{OH})_2^{st}]^-$	-1941.6221	-1941.3289	1.3	0.7
$^1[(\text{OPO})_{\text{H}}^f\text{V}^{\text{III}}(\text{H}_2\text{O})^s(\text{OH})_2^{ct}]^-$	-1941.5798	-1941.2804	31.8	31.1
$^3[(\text{OPO})_{\text{H}}^f\text{V}^{\text{III}}(\text{H}_2\text{O})^s(\text{OH})_2^{ct}]^-$	-1941.6323	-1941.3331	-1.3	-2.0

Species	E_{gas}	G_{aq}	$G_{\text{rel}}(\text{pH}=0)$	$G_{\text{rel}}(\text{pH}=7)$
$^1[(OPO)_H^f V^{III}(H_2O)^t(OH)_2^{cs}]^-$	-1941.6015	-1941.3001	19.4	18.8
$^3[(OPO)_H^f V^{III}(H_2O)^t(OH)_2^{cs}]^-$	-1941.6254	-1941.3234	4.8	4.1

Table 4.4. Comprehensive compilation of all $(OPO)V^{III}$ species containing only oxo/hydroxo/aqua ligands studied, along with their gas-phase energies (E_{gas}) and aqueous free energies (G_{aq}), both in hartrees. The last two columns show their aqueous free energies, in kcal/mol, relative to the ground states at pH 0 and 7 ($(OPO)_H^f V^V O^c(OH)^s(H_2O)^t$ and $[(OPO)^f V^V O^c(OH)_2^{st}]^{2-}$, respectively). For some entries, geometry optimization led to the formation of a lower-energy isomer. The energies for these entries are not reported.

Species	E_{gas}	G_{aq}	$G_{\text{rel}}(\text{pH}=0)$	$G_{\text{rel}}(\text{pH}=7)$
$^3(OPO)^f V^{III}(HOiPr)^c(H_2O)_2^{st}$	-1907.1454	-1906.7524	-12.8	-3.9
$^3(OPO)^f V^{III}(HOiPr)^s(H_2O)_2^{ct}$	-1907.1518	-1906.7610	-18.2	-9.3
$^3(OPO)^f V^{III}(HOiPr)^t(H_2O)_2^{cs}$	-1907.1489	-1906.7546	-14.2	-5.3
$^3(OPO)_H^f V^{III}(HOiPr)^c(OH)^s(H_2O)^t$	-1907.1417	-1906.7463	-9.0	-0.1
$^3(OPO)_H^f V^{III}(HOiPr)^c(OH)^t(H_2O)^s$	-1907.1398	-1906.7456	-8.6	0.3
$^3(OPO)_H^f V^{III}(HOiPr)^s(OH)^c(H_2O)^t$	-1907.1520	-1906.7574	-16.0	-7.1
$^3(OPO)_H^f V^{III}(HOiPr)^s(OH)^t(H_2O)^c$	-1907.1339	-1906.7422	-6.5	2.4
$^3(OPO)_H^f V^{III}(HOiPr)^t(OH)^c(H_2O)^s$	-1907.1472	-1906.7494	-10.9	-2.0
$^3(OPO)_H^f V^{III}(HOiPr)^t(OH)^s(H_2O)^c$	-1907.1439	-1906.7503	-11.5	-2.6
$^3(OPO)_H^f V^{III}(OiPr)^c(H_2O)_2^{st}$	-1907.1448	-1906.7528	-13.1	-4.2
$^3(OPO)_H^f V^{III}(OiPr)^s(H_2O)_2^{ct}$	-1907.1544	-1906.7567	-15.5	-6.6
$^3(OPO)_H^f V^{III}(OiPr)^t(H_2O)_2^{cs}$	-1907.1454	-1906.7458	-8.7	0.2
$^3[(OPO)^f V^{III}(HOiPr)^c(OH)^s(H_2O)^t]^-$	-1906.6425	-1906.3086	-4.6	-5.2
$^3[(OPO)^f V^{III}(HOiPr)^c(OH)^t(H_2O)^s]^-$	-1906.6463	-1906.3113	-6.3	-6.9
$^3[(OPO)^f V^{III}(HOiPr)^s(OH)^c(H_2O)^t]^-$	-1906.6475	-1906.3125	-7.1	-7.7
$^3[(OPO)^f V^{III}(HOiPr)^s(OH)^t(H_2O)^c]^-$	-1906.6369	-1906.3039	-1.7	-2.3
$^3[(OPO)^f V^{III}(HOiPr)^t(OH)^c(H_2O)^s]^-$	-1906.6436	-1906.3069	-3.6	-4.2

| Species	E_{gas}	G_{aq}	$G_{rel}(pH = 0)$	$G_{rel}(pH = 7)$
$^3[(OPO)^f V^{III}(HOiPr)^t(OH)^s(H_2O)^c]^-$	-1906.6461	-1906.3043	-1.9	-2.6
$^3[(OPO)^f V^{III}(OiPr)^c(H_2O)_2^{st}]^-$	-1906.6476	-1906.3131	-7.5	-8.1
$^3[(OPO)^f V^{III}(OiPr)^s(H_2O)_2^{ct}]^-$	-1906.6425	-1906.3043	-1.9	-2.5
$^3[(OPO)^f V^{III}(OiPr)^t(H_2O)_2^{cs}]^-$	-1906.6420	-1906.2957	3.4	2.8
$^3[(OPO)_H^f V^{III}(HOiPr)^c(OH)_2^{st}]^-$	geometry unstable			
$^3[(OPO)_H^f V^{III}(HOiPr)^s(OH)_2^{ct}]^-$	-1906.6284	-1906.2897	7.2	6.6
$^3[(OPO)_H^f V^{III}(HOiPr)^t(OH)_2^{cs}]^-$	-1906.6261	-1906.2951	3.8	3.2
$^3[(OPO)_H^f V^{III}(OiPr)^c(OH)^s(H_2O)^t]^-$	-1906.6346	-1906.2971	2.6	1.9
$^3[(OPO)_H^f V^{III}(OiPr)^s(OH)^c(H_2O)^t]^-$	-1906.6346	-1906.3005	0.5	-0.2
$^3[(OPO)_H^f V^{III}(OiPr)^s(OH)^c(H_2O)^t]^-$	-1906.6482	-1906.3055	-2.7	-3.3
$^3[(OPO)_H^f V^{III}(OiPr)^s(OH)^t(H_2O)^c]^-$	-1906.6398	-1906.2991	1.4	0.7
$^3[(OPO)_H^f V^{III}(OiPr)^t(OH)^c(H_2O)^s]^-$	geometry unstable			
$^3[(OPO)_H^f V^{III}(OiPr)^t(OH)^s(H_2O)^c]^-$	geometry unstable			

Table 4.5. Compilation of all $(OPO)V^{III}(OiPr)$ species studied, with only six-coordinate *fac*-(OPO) triplet complexes considered. The second and third columns show the gas-phase energies (E_{gas}) and aqueous free energies (G_{aq}), both in hartrees. The last two columns show their aqueous free energies, in kcal/mol, relative to the ground states at pH 0 and 7 ($(OPO)_H^f V^V O^c(OH)^s(H_2O)^t$ and $[(OPO)^f V^V O^c(OH)_2^{st}]^{2-}$, respectively). For some entries, geometry optimization led to the formation of a lower-energy isomer. The energies for these entries are not reported.

At pH 0, the lowest energy $(OPO)V^{III}(OiPr)$ species is $^3(OPO)^f V^{III}(HOiPr)^s(H_2O)_2^{ct}$ at -18.2 kcal/mol relative to the starting $(OPO)_H^f V^V O^c(OH)^s(H_2O)^t$, whereas the lowest energy $(OPO)V^{III}$ species without any isopropoxy groups is $^3(OPO)^f V^{III}(H_2O)_3^{cst}$ at -17.7 kcal/mol relative to $(OPO)_H^f$-$V^V O^c(OH)^s(H_2O)^t$. Furthermore, the lowest energy five-coordinate $(OPO)V^{III}$ species without any isopropoxy groups is $^3(OPO)_H V^{III}(OH)^s(H_2O)^a$ at -7.9 kcal/mol relative to $(OPO)_H^f V^V O^c(OH)^s$-$(H_2O)^t$, indicating that it is possible for $^3(OPO)^f V^{III}(HOiPr)^s(H_2O)_2^{ct}$ and $^3(OPO)^f V^{III}(H_2O)_3^{cst}$ to interconvert *via* a labile isopropanol ligand. These three species are shown in detail in Figure 4.21. Note that at pH 7 the same three species are still the most stable, but with energies of -9.3, -8.8, and 1.0 kcal/mol with respect to $[(OPO)^f V^V O^c(OH)_2^{st}]^{2-}$, respectively.

4.5.7 Catalytic cycle involving H-atom abstraction followed by isopropyl addition

By considering the lowest energy configurations of the various V^V, V^{IV}, and V^{III} intermediates and transition states, we can now construct a catalytic cycle that features both H-atom abstraction

Figure 4.21. The geometry-optimized structures of $^3(\text{OPO})^f\text{V}^{\text{III}}(\text{HO}i\text{Pr})^s(\text{H}_2\text{O})_2^{ct}$, $^3(\text{OPO})^f\text{V}^{\text{III}}(\text{H}_2\text{O})_3^{cst}$, and $^3(\text{OPO})_{\text{H}}\text{V}^{\text{III}}(\text{OH})^s(\text{H}_2\text{O})^a$. These are the most stable $(\text{OPO})\text{V}^{\text{III}}(\text{O}i\text{Pr})$ species, and six and five coordinate $(\text{OPO})\text{V}^{\text{III}}$ species, respectively, at both pH 0 and 7.

$$^3(\text{OPO})^f\text{V}^{\text{III}}(\text{HO}i\text{Pr})^s(\text{H}_2\text{O})_2^{ct} \qquad ^3(\text{OPO})^f\text{V}^{\text{III}}(\text{H}_2\text{O})_3^{cst} \qquad ^3(\text{OPO})_{\text{H}}\text{V}^{\text{III}}(\text{OH})^s(\text{H}_2\text{O})^a$$
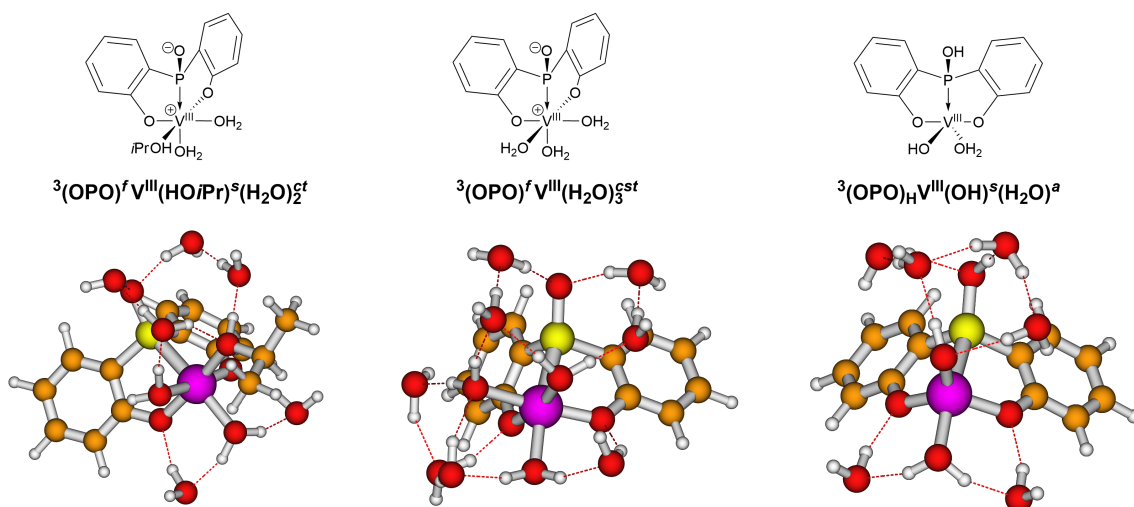
from propane and isopropyl radical trapping before reoxidation. This cycle is shown in Scheme 4.3. The first part, involving isomerization of the starting $(\text{OPO})_{\text{H}}^f\text{V}^{\text{V}}\text{O}^c(\text{OH})^s(\text{H}_2\text{O})^t$ to $(\text{OPO})^f\text{V}^{\text{V}}\text{O}^c$-$(\text{H}_2\text{O})_2^{st}$, followed by C−H activation to $(\text{OPO})_{\text{H}}^f\text{V}^{\text{IV}}\text{O}^c(\text{H}_2\text{O})_2^{st}$, is identical to that of Scheme 4.2. However, instead of being immediately reoxidized as in Scheme 4.2, the V^{IV} species traps the generated isopropyl radical to form a $\text{V}^{\text{III}}(\text{O}i\text{Pr})$ species. One example of such a pathway is shown in Scheme 4.3, in which the $(\text{OPO})_{\text{H}}^f\text{V}^{\text{IV}}\text{O}^c(\text{H}_2\text{O})_2^{st}$ species first isomerizes to the slightly higher (at 15.4 kcal/mol relative to the starting V^{V} complex) $(\text{OPO})_{\text{H}}^f\text{V}^{\text{IV}}\text{O}^s(\text{H}_2\text{O})_2^{ct}$, which then combines with the isopropyl radical to form $^3(\text{OPO})_{\text{H}}^f\text{V}^{\text{III}}(\text{O}i\text{Pr})^s(\text{H}_2\text{O})_2^{ct}$ at −15.5 kcal/mol, which readily isomerizes to $^3(\text{OPO})^f\text{V}^{\text{III}}(\text{HO}i\text{Pr})^s(\text{H}_2\text{O})_2^{ct}$, the lowest energy $\text{V}^{\text{III}}(\text{O}i\text{Pr})$ species at −18.2 kcal/mol relative to the starting $(\text{OPO})_{\text{H}}^f\text{V}^{\text{V}}\text{O}^c(\text{OH})^s(\text{H}_2\text{O})^t$. Loss of the HO$i$Pr product to form the five coordinate species $^3(\text{OPO})\text{V}^{\text{III}}(\text{H}_2\text{O})_2^{sa}$ (at −1.5 kcal/mol) is uphill but not insurmountably so, and recoordination of an aqua ligand to the sixth coordination site to form $^3(\text{OPO})^f\text{V}^{\text{III}}(\text{H}_2\text{O})_3^{cst}$ recovers (at −17.7 kcal/mol) most of this energy. As the overall reaction $\text{C}_3\text{H}_8 + \frac{1}{2}\text{O}_2 \longrightarrow \text{HO}i\text{Pr}$ has $\Delta G = -31.2$ kcal/mol, reoxidation of $^3(\text{OPO})\text{V}^{\text{III}}(\text{H}_2\text{O})_2^{sa}$ to $(\text{OPO})^f\text{V}^{\text{V}}\text{O}^c(\text{H}_2\text{O})_2^{st}$ (assuming that O_2 is the terminal oxidation) is downhill by 11.9 kcal/mol.

4.5.8 Comparison of the catalytic cycles

The H-atom abstraction-only pathway results in the dehydrogenation of propane to form propylene. However, as this is significantly uphill ($\text{C}_3\text{H}_8 \longrightarrow \text{C}_3\text{H}_6 + \text{H}_2$, $\Delta G = 20.3$ kcal/mol), it is unlikely unless some oxidant is coupled to the reaction. Coupling dehydrogenation with dioxygen greatly
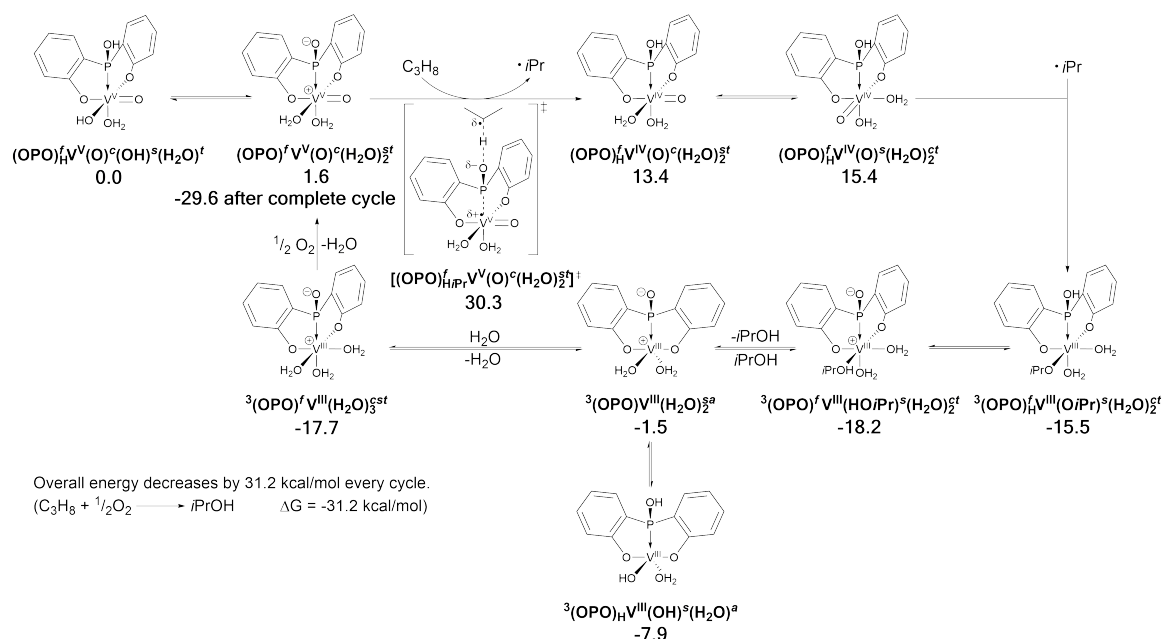
Scheme 4.3. A potential catalytic cycle that assumes that the isopropyl radical adds to the vanadium oxo, reducing it to V^{III}. This assumption derives from the behavior of the heterogeneous VPO catalyst. All energies are in kcal/mol. Note that the overall reaction in this cycle is $C_3H_8 + {}^1/_2O_2 \longrightarrow HOiPr$, with $\Delta G = -31.2$ kcal/mol. Hence, whereas the $(OPO)^f V^V O^c(H_2O)_2^{st}$ complex is initially 1.6 kcal/mol above the starting state, after one complete cycle it is -29.6 kcal/mol below the starting state.

increases its favorability, for a ΔG of -32.3 kcal/mol. We have not found any large barriers in the H-atom abstraction-only pathway that might preclude the production of propylene and water as in the overall equation $C_3H_8 + \frac{1}{2}O_2 \longrightarrow C_3H_6 + H_2O$; however, we note that our results do not include the details of how the one-electron oxidation of $[(OPO)^f V^{IV}(O)^c(H_2O)_2^{st}]^-$ or $[(OPO)^f V^{IV}(O)^s(H_2O)_2^{ct}]^-$ takes place and how the released electron is transferred to dioxygen to ultimately form water. Such a mechanism may involve an inner sphere coordination of dioxygen to form a V^V superoxo intermediate and may involve further $C-H$ activation by this superoxide. Given the reduction potential of dioxygen versus that of $[(OPO)^f V^{IV}(O)^c(H_2O)_2^{st}]^-$ or $[(OPO)^f V^{IV}(O)^s(H_2O)_2^{ct}]^-$ (1.23 V versus 0.77 V or 1.07 V), we believe that the H-atom abstraction-only pathway will be viable and productive in the absence of lower-energy alternative pathways.

Comparing the H-atom abstraction-only versus the H-atom abstraction and isopropyl addition pathways, we note that the branching point is the monohydrogenated complexes $(OPO)_H^f V^{IV}(O)$- $(H_2O)_2$, which may either undergo reoxidation as in the abstraction-only mechanism (Scheme 4.2), or add the isopropyl radical (Scheme 4.3). The former overall is thermodynamically downhill by 0.8 kcal/mol in the lowest isomers; whereas the latter is thermodynamically downhill by 30.9 kcal/mol in one simple elementary step with an intuitively minimal barrier. Hence, the catalytic cycle involving isopropyl addition appears to be more likely to occur than the cycle that only features H-atom

abstraction. As in the H-atom abstraction-only case, we have not considered the precise nature of the reoxidation step. However, we anticipate that it may also involve inner sphere coordination of dioxygen, in which case a V^V η^2-peroxo intermediate is formed. This would be analogous to the heterogeneous VPO system, and we would also need to anticipate C$-$H activation by these peroxide species as well.

4.6 Conclusions

We have identified a new mechanistic motif, which we call the reductive-coupled oxo activation mechanism, in which a normally unreactive main-group oxo becomes a potent hydrogen atom abstractor when coupled to a transition metal (in our case V^V or Mo^{VI}). The new activity of this oxo, which we quantify using the O$-$H dissociation parameter D_H, is modified from that of the transition metal oxo itself and may be significantly higher for certain elements, specifically phosphorous in the +V oxidation state and selenium and tellurium in the +IV and +VI oxidation states. Our results are consistent with existing experimental and theoretical mechanistic work on the n-butane to maleic anhydride VOPO catalyst. We believe that knowledge of this new mechanistic motif will allow for the *de novo* rational design of future oxidation catalysts.

As a showcase of the power of the ROA mechanistic motif, we have designed a potential inorganic complex $(OPO)^f_H V^V O^c (OH)^s (H_2O)^t$ that may serve as a homogeneous oxidation catalyst for alkanes. We have identified catalytic cycles for the oxidation of propane to propylene or isopropanol. Our likely catalytic cycle involves H-atom abstraction from propane, followed by recombination of the produced isopropyl radical and V^{IV} species to form a V^{III} isopropoxy species. Ligand exchange results in the formation of free isopropanol and reoxidation regenerates the starting V^V species. Our theoretical results are encouraging for us to continue our computational work in investigating reoxidation pathways, and to commence experimental work.

4.7   References

[1] Centi, G.; Trifiro, F.; Ebner, J. R.; Franchetti, V. M. *Chem. Rev.* **1988**, *88*, 55–80.

[2] Hodnett, B. K. *Heterogeneous Catalytic Oxidation.* Wiley: New York, **2000**.

[3] Cheng, M.-J. and Goddard, W. A. *J. Am. Chem. Soc.* **2013**, *135*, 4600–4603.

[4] Schuurman, Y.; Gleaves, J. T. *Ind. Eng. Chem. Res.* **1994**, *33*, 2935–2941.

[5] Hutchings, G. J.; Desmartinchomel, A.; Olier, R.; Volta, J. C. *Nature* **1994**, *368*, 41–45.

[6] Cheng, M.-J.; Goddard, W. A.; Fu, R. *Methods for providing bond activation catalysts and related catalysts, systems, and methods.* U.S. Patent application 14/192,856, filed February 27, **2014**. Patent pending.

[7] Marino, N.; Hanson, S. K.; Müller, P.; Doyle, R. P. *Inorg. Chem.* **2012**, *51*, 10077–10079.

[8] Herron, N.; Thorn, D. L.; Harlow, R. L.; Coulston, G. W. *J. Am. Chem. Soc.* **1997**, *119*, 7149–7150.

[9] Solis-Ibarra, D.; Silvia, J. S.; Jancik, V.; Cummins, C. C. *Inorg. Chem.* **2011**, *50*, 9980–9984.

[10] Pan, B. F.; Bezpalko, M. W.; Foxman, B. M.; Thomas, C. M. *Organometallics* **2011**, *30*, 5560–5563.

[11] (a) Derrah, E. J.; Martin, C.; Mallet-Ladeira, S.; Miqueu, K.; Bouhadir, G.; Bourissou, D. *Organometallics* **2013**, *32*, 1121–1128.

(b) Derrah, E. J.; Ladeira, S.; Bouhadir, G.; Miqueu, K.; Bourissou, D. *Chem. Commun.* **2011**, *47*, 8611–8613.

[12] (a) Pan, B. F.; Bezpalko, M. W.; Foxman, B. M.; Thomas, C. M. *Dalton Trans.* **2012**, *41*, 9083–9090.

(b) Bauer, R. C.; Gloaguen, Y.; Lutz, M.; Reek, J. N. H.; Bruin, B. de; Vlugt, J. I van der. *Dalton Trans.* **2011**, *40*, 8822–8829.

(c) Mazzeo, M. Lamberti, M.; Massa, A.; Scettri, A.; Pellecchia, C.; Peters, J. C. *Organometallics* **2008**, *27*, 5741–5743.

(d) Mazzeo, M.; Strianese, M.; Kuhl, O.; Peters, J. C. *Dalton Trans.* **2011**, *40*, 9026–9033.

[13] Gloaguen, Y.; Jacobs, W.; Bruin, B. de; Lutz, M.; Vlugt, J. I. van der; *Inorg. Chem.* **2013**, *52*, 1682–1684.

[14] *Jaguar, version 7.9*; Schrödinger, LLC: **2012**, New York, NY.

[15] (a) Tannor, D. J.; Marten, B.; Murphy, R.; Friesner, R. A.; Sitkoff, D.; Nicholls, A.; Ringnalda, M.; Goddard, W. A.; Honig, B. *J. Am. Chem. Soc.* **1994**, *116*, 11875–11882.

(b) Marten, B.; Kim, K.; Cortis, C.; Friesner, R. A.; Murphy, R. B.; Ringnalda, M. N.; Sitkoff, D.; Honig, B. *J. Phys. Chem.* **1996**, *100*, 11775–11788.

[16] Sears, F. W.; Zemansky, M. W.; Young, H. D. *University Physics, 6th Ed.*; Addison-Wesley, **1982**.

[17] The probe radius r is automatically calculated by *Jaguar* using the formula $r = 0.5833 \sqrt[3]{MW/\rho}$ where MW is the molecular weight and ρ is the density of the solvent.

[18] (a) Becke, A. D. *Phys. Rev. A.* **1998**, *38*, 3098–3100.

(b) Becke, A. D. *J. Chem. Phys.* **1993**, *98*, 5648–5652.

(c) Lee, C. T.; Yang, W. T.; Parr, R. G. *Phys. Rev. B.* **1988**, *37*, 785–789.

[19] Hay, P. J.; Wadt, W. R. *J. Chem. Phys.* **1985**, *82*, 299–310.

[20] (a) Hay, P. J.; Wadt, W. R. *J. Chem. Phys.* **1985**, *82*, 270–283;

(b) Hay, P. J.; Wadt, W. R. *J. Chem. Phys.* **1985**, *82*, 284–298.

[21] (a) Hehre, W. J.; Ditchfield, R; Pople, J. A. *J. Chem. Phys.* **1972**, *56*, 2257–2261.

(b) Francl, M. M.; Pietro, W. J.; Hehre, W. J.; Binkley, J. S.; Gordon, M. S.; Defrees, D. J.; Pople, J. A. *J. Chem. Phys.* **1982**, *77*, 3654–3665.

[22] Tissandier, M. D.; Cowen, K. A.; Feng, W. Y.; Gundlach, E.; Cohen, M. H.; Earhart, A. D.; Coe, J. V.; Tuttle, T. R. *J. Phys. Chem. A.* **1998**, *102*, 7787–7794. Calculated at standard conditions.

[23] Wertz, D. H. *J. Am. Chem. Soc.* **1980**, *102*, 5316–5322.

[24] Bridgeman, O.C.; Aldrich, E.W. *J. Heat Transfer* **1964**, *86*, 279–286.

[25] Pangborn, A. B.; Giardello, M. A.; Grubbs, R. H.; Rosen, R. K.; Timmers, F. J. *Organometallics* **1996**, *15*, 1518–1520.

[26] Bartlett, P. D. *Rec. Chem. Prog.* **1950**, *11*, 47–51.

[27] (a) Wife, R. L.; Oort, A. B. van; Doorn, J. A. van; Leeuwen, P. W. N. M. van *Synthesis* **1983**, 71.

(b) Baccolini, G.; Bazzocchi, M.; Carla, B. *Eur. J. Org. Chem.* **2001**, 2229–2233.

[28] Some recent publications that show similar chemistry of using VOCl₃ to install hard multidentate anionic ligands onto vanadium include:
(a) Kurmaev, D. A.; Kolosov, N. A.; Gagieva, S. C.; Borissova, A. O.; Tuskaev, V. A.; Bravaya, N. M.; Bulychev, B. M. *Inorg. Chim. Acta* **2013**, *396*, 136–143.

(b) Villanneau, R.; ben Djamâa, A.; Chamoreau, L.-M.; Gontard, G.; Proust, A. *Eur. J. Inorg. Chem.* **2013**, 1815–1820.

(c) Tong, L. H.; Wong, Y.-L.; Lee, H. K.; Dilworth, J. R. *Inorg. Chim. Acta* **2012**, *383*, 91–97.

(d) North, M.; Stewart, E. L.; Young, C. *Tetrahedron: Asymmetry* **2012**, *23*, 1218–1225.

[29] Wolff, F.; Choukroun, R.; Lorber, C.; Donnadieu, B. *Eur. J. Inorg. Chem.* **2003**, 628–632.

[30] Romanowski, G. *J. Mol. Cat. A: Chemical* **2013**, *368*, 137–144.

[31] Busacca, C. A.; Lorenz, J. C.; Grinberg, N.; Haddad, N.; Hrapchak, M.; Latli, B.; Lee, H.; Sabila, P.; Saha, A.; Sarvestani, M.; Shen, S.; Varsolona, R.; Wei, X.; Senanayake, C. H. *Org. Lett.* **2005**, *7*, 4277–4280.

[32] Bickelhaupt, F.; van der Does, T. *Biphosphine production.* U.S. Patent US4874897 A, **1989**.

[33] Doorn, J. A. van; Frijns, J. H. G.; Meijboom, N. *Recl. Trav. Chim. Pays-Bas* **1991**, *110*, 441–449.